EUROPEAN COMMISSION

Community Research

SEVENTH FRAMEWORK PROGRAMME

ARCHER

Collaborative Project (CP)

Co-funded by the European Commission under the Euratom Research and Training Programme on Nuclear Energy within the Seventh Framework Programme

Grant Agreement Number : 269892

Start date : 01/02/2011 Duration : 48 Months

www.archer-project.eu

SiC coatings and Ag diffusion

Authors : ROHBECK Nadia (UNIMAN) , X. Geng, P. Xiao, A. Reinicke, M. Lustfeld, W. Lippmann

ARCHER - Contract Number: 269892
Advanced High-Temperature Reactors for Cogeneration of Heat and Electricity R&D
EC Scientific Officer: Dr. Panagiotis Manolatos

Document title	SiC coatings and Ag diffusion
Author(s)	ROHBECK Nadia , X. Geng, P. Xiao, A. Reinicke, M. Lustfeld, W. Lippmann
Number of pages	52
Document type	Deliverable
Work Package	WP 31
Document number	D31.21
Issued by	NRG
Date of completion	03/11/2014
Dissemination level	Confidential, only for members of the consortium (including the Commission Services).

Summary

The pulsed laser deposition process (TU Dresden) was successfully applied to fabricate subsequent coating layers of silver and SiC on spherical ZrO2 kernels with the aim to allow studying silver diffusion through SiC coatings on non-active simulated fuel kernels. The deposition of dense silver coatings that were free of droplets and impurities was accomplished. However, the subsequent deposition of high quality SiC coatings proved to be challenging. Crack and bubble formation, insufficient crystallinity and non-stoichiometry were issues that required adjustments in the experimental set-up (high vacuum) and an extensive parameter study of the deposition conditions (e.g. pulse frequency and energy, temperature). Ultimately, crack-free and nanocrystalline SiC coatings were successfully deposited onto silver-coated zirconia kernels. A fundamental study (UMAN) of the interactions of silver and SiC showed that in its liquid state silver dissolves SiC by forming a silver-silicon alloy and a separate carbon phase. This reaction is partly reversible and leads to the formation of ?-SiC independent of the original SiC polytype. Tests including silver containing TRISO particles showed that silver penetrates the SiC coating rapidly and in large quantities causes recrystallization of SiC grains. These observations were validated by thermodynamic calculations. Hence a completely novel approach to look at the cause of silver release from intact SiC coatings in TRISO fuel is proposed within this report. This migration mechanism that is founded on a reaction might be unavoidable, but could still be mitigated by careful engineering of the SiC microstructure since grain boundary characteristics will influence the silver release rates observed in irradiation experiments.

Approval

Date	By
04/11/2014	Steven KNOL
05/11/2014	Mathias LAURIE
03/12/2014	Steven KNOL

Distribution list

Name	Organisation	Comments
P. Manolatos	EC DG RTD	Through the EC participant portal
All beneficiaries	ARCHER	Through the private online workspace

ARCHER project – Contract Number: 269892

Advanced High-Temperature Reactors for Cogeneration of Heat and Electricity R&D

EC Scientific Officer: Dr. Panagiotis Manolatos

Document title	SiC properties and fission product diffusion
Author(s)	UMAN: Nadia Rohbeck, Xin Geng, Ping Xiao TU Dresden: Anne-Maria Reinecke, Martin Lustfeld, Wolfgang Lippmann
Number of pages	52
Document type	Deliverable
Work Package	WP31
Document number	D31.21-v1
Issued by	UMAN
Date of completion	02/10/14
Dissemination level	Restricted to the partners of the ARCHER project

Summary

The pulsed laser deposition process (TU Dresden) was successfully applied to fabricate subsequent coating layers of silver and SiC on spherical ZrO_2 kernels with the aim to allow studying silver diffusion through SiC coatings on non-active simulated fuel kernels. The deposition of dense silver coatings that were free of droplets and impurities was accomplished. However, the subsequent deposition of high quality SiC coatings proved to be challenging. Crack and bubble formation, insufficient crystallinity and non-stoichiometry were issues that required adjustments in the experimental set-up (high vacuum) and an extensive parameter study of the deposition conditions (e.g. pulse frequency and energy, temperature). Ultimately, crack-free and nanocrystalline SiC coatings were successfully deposited onto silver-coated zirconia kernels.

A fundamental study (UMAN) of the interactions of silver and SiC showed that in its liquid state silver dissolves SiC by forming a silver-silicon alloy and a separate carbon phase. This reaction is partly reversible and leads to the formation of β-SiC independent of the original SiC polytype. Tests including silver containing TRISO particles showed that silver penetrates the SiC coating rapidly and in large quantities causes recrystallization of SiC

grains. These observations were validated by thermodynamic calculations. Hence a completely novel approach to look at the cause of silver release from intact SiC coatings in TRISO fuel is proposed within this report. This migration mechanism that is founded on a reaction might be unavoidable, but could still be mitigated by careful engineering of the SiC microstructure since grain boundary characteristics will influence the silver release rates observed in irradiation experiments.

Approval

Rev.	Short description	First author	WP Leader	SP leader	Coordinator
0	First issue	Nadia Rohbeck (UMAN) 02/10/14	Steven Knol (NRG)	Mathias Laurie (ITU)	Steven Knol ../../..

Distribution list

Name	Organisation	Comments
P. Manolatos	EC DG RTD	
All technical participants	ARCHER	
Steering Committee members	ARCHER	

Table of contents

1 Pulsed Laser Deposition of SiC coatings at TU Dresden

1.1 Introduction

Within the framework of the ARCHER (Advanced High-Temperature Reactors for Cogeneration of Heat and Electricity R&D) EU research program “Fuel and Fuel Cycle” area, a laser-assisted physical coating process for preparing SiC barrier layers and B_4C coatings has been developed and applied to supplement the previously used chemical process of chemical vapor deposition (CVD).

Deliverable 31.21 was aimed at performing fundamental investigations on silver diffusion in TRISO-coated particles. The task of TU Dresden was to prepare silver coatings on spherical Al_2O_3 and ZrO_2 particles by means of pulsed laser deposition (PLD). The spherical particles were supplied by the University of Manchester (UMAN) and, following silver coating at TU Dresden, coated with SiC in a CVD system at UMAN. To prevent premature evaporation of the silver coating during the CVD process, which was carried out at 1600 °C, an additional thin SiC protective layer was applied to the silver coating via PLD.

1.2 State of the Art

The pulsed laser deposition (PLD) technology was first used and described in 1965 by Smith and Turner in Rochester, New York, for manufacturing semiconductors and dielectric coatings [1]. The process was characterized by use of a ruby laser, which, unlike the prior process of vapor deposition, enabled material removal via short pulses (≈ 1 µs) as well as free selection of the coating atmosphere by allowing the radiation to be guided from the outside to the receiver and hence the energy source to be placed outside the deposition chamber. The process only became established in 1987 through the work of T. Venkatesan et al. [2] and the development of excimer lasers with considerably shorter pulse times (20 ns). Vekatesan et al. uncovered a key characteristic of the PLD process: Due to the short pulse time, stoichiometric transfer of the target material to the substrate was possible. In a concrete example, supraconductive coatings from the $YBa_2Cu_3O_{7-\delta}$ system were deposited with the exact same stoichiometry. In subsequent years, the PLD technology started being used for a large number of metals, alloys, and other chemical compounds, including plastics. Because of the relatively high investment costs for the excimer laser system, the application was primarily restricted to high-grade optical

coatings and functional coatings such as semiconductor coatings in microelectronics [4][5], multioxide coatings as supraconductors [6], and wear-resistant coatings [7][8][20].

Coatings with silver are made on a large scale using electrochemical methods, sometimes supported by a voltage source. Physical coating methods are primarily used for coatings with functional requirements. For example, sputtering methods are used to apply silver coatings to flat glass in flat glass production plants to enable adjustment of the optical properties, especially reflection. However, in the recent past, PLD systems have been developed, tested, and commercially used to supplant these processes [9][10]. Research has been focused on deposition of silver particles with precisely defined sizes, shapes, and separation distances by PLD [21], with special interest being paid to the differences in optical properties of classic bodies and metal particles that are considerably smaller than the wavelengths of visible light. Especially the sharply delineated absorption bands can be utilized in a multitude of special technological processes [21][22][23][24][25]. Attempts have been made to deposit individual particles, islands, or coatings with thicknesses of a few nanometers. Coatings of thickness greater than 100 nm are used in medical technology, where, for instance, the antibacterial activity of silver is utilized in coatings on medical devices and implants, primarily made of titanium alloys [26][27][28]. Research in this area has centered on surface properties and alloying with additives or the base material. In contrast, large-scale industrial process solutions for plasma coating of spherical particles with silver in vacuum conditions are not known.

Over the last 15 years SiC coatings have been investigated and implemented on single-crystal silicon or on sapphire due to their interesting electronic and electromechanical properties [11][12][13][14][15][16][17][18][19]. Investigations have mainly been centered on particulate-free, homogeneous coatings. The deposition temperature of between 250 °C and 1100 °C was identified as a key parameter for the resultant coating properties (especially crystal modifications and coating stresses). The coatings were found to exhibit long-range crystalline order starting at a temperature of about 600 °C to 800 °C. Possibilities for reducing stresses, mainly through heat treatment, were also discussed [7][8]. The deposited coatings were less than 500 nm thick in all cases except in the application discussed by Zehnder et al. [11]. In this case, strongly bonded coatings of thickness greater than 5 μm were deposited onto 300-nm-thick silicon substrates and the stresses in the coatings were calculated based on the curvature of the coated sample. There is no information on PLD coatings of SiC on silver in the literature as of yet.

1.3 Evaluation of Process-Determining Parameters Based on In-House Knowledge of Coating of Planar Substrates

The quality of the coating deposited onto planar substrates using PLD technology can be affected by a large number of parameters that define the laser beam, the process, and the working environment.

1.3.1 Pulse Energy

Knowing the precise laser energy input over the duration of the process is key to being able to interpret the measurement results. The laser pulse energy measured directly in front of the target was adjusted to a maximum value of 410 mJ. Laser beam irradiation of a target with an area of 1.5 x 1.3 mm² yielded a maximum homogeneous energy density of 20 J/cm², much greater than the SiC ablation threshold of approx. 1 J/cm² [16]. This pulse energy is only available at the beginning of a coating test. The setup with the target at a 45° angle to the laser beam used in this work caused secondary coating of the coupling window and hence a reduction in the window transmission. This effect was investigated within the scope of this work and is illustrated in Figure 1-1 in the form of the results of 22 tests. According to the results, for a total energy input of 50 kJ, the pulse energy drops by up to 50% during the coating test. On the other hand, ablation at low pulse energy can lead to “window cleaning effects,” providing an explanation for the occurrence of the two negative values.

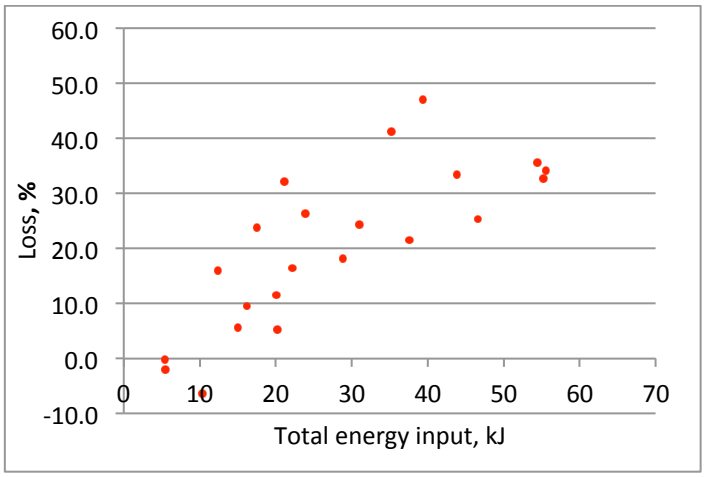

Figure 1-1: Loss of laser beam energy as a function of total energy input for one coating cycle

The amplitude of the pulse energy directly affected the deposition rate, a main factor characterizing the effectiveness of the process in terms of the coating thickness in relation to the coating time. Deposition rates of up to 8 nm/s were achieved.

1.3.2 Pulse Frequency

The pulse frequency can be varied from 1 Hz to 40 Hz. It affects the deposition rate (the coating growth rate is proportional to the number of pulses per second) and the degree of pulse overlapping on the target, which also depends on the rotational speed of the target.

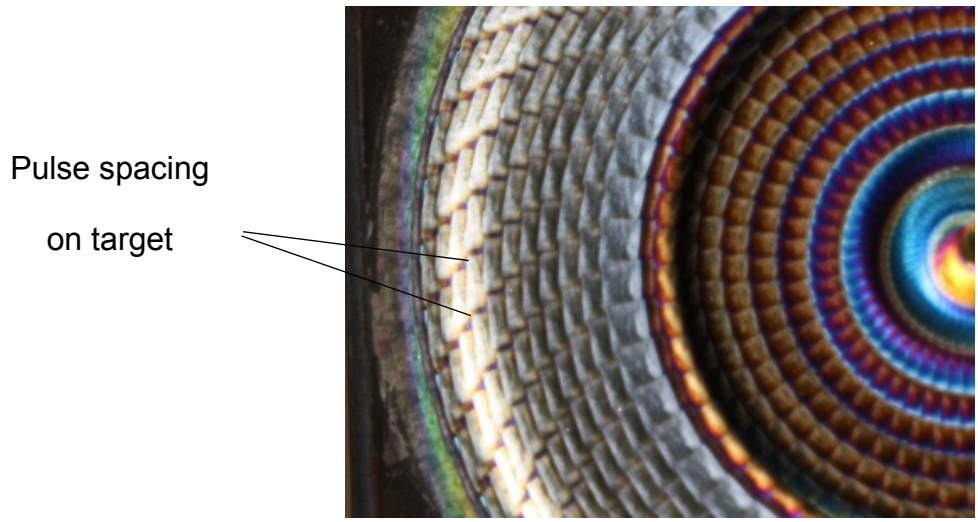

Figure 1-2: Arrangement of laser pulses on target, influenced by pulse frequency and nonlinear rotational speed

Pulse frequency and rotational speed of the target were selected to minimize pulse overlapping (Figure 1-2). The greater the amount of pulse overlapping, the higher the specific heat input into the target. This can force the formation of a melt or spalling, in which particles are detached from the target due to recoil forces and are deposited unintendedly in the form of droplets or particulates onto the substrate.

1.3.3 Focal Length

The correct name for the smallest attainable spot after the focusing optics in an excimer laser is not the “focus,” but rather a “projection.” This is based on the way in which the beam is generated and the optics used for beam shaping. Ablation with a defocused laser beam is not recommended because an inhomogeneous intensity profile prevails under these conditions. The projected image of the laser beam described a rectangle with dimensions of approximately 1.5 x 1.3 mm². The focusing optics had a focal length of 400 mm.

1.3.4 Distance Between Target and Substrate

The target and the substrate are aligned parallelly. By varying the distance between substrate and coating, the kinetic energy of the ablated particles impinging on the substrate can be adjusted as well as the mean coating thickness, and the coating thickness distribution on the substrate. At the time of ablation, the components of the target (atoms, ions, and electrons) are accelerated in a direction normal to the target by expansion of the plasma and decelerated on their way to the substrate by collisions with each other due to their different speeds or with components of the working atmosphere. Hence, the particles are first accelerated after exiting the target and then decelerated more and more as they approach the substrate as a function of the vacuum properties. The kinetic energy of the impinging particles can be so high that coating deposition is made impossible by the superimposed sputter effect. Due to the limitations imposed by the construction, the target-to-substrate spacing could be varied in the range between 30 mm and 70 mm. Based on recommendations given in the literature, a spacing of 40 mm was selected.

Figure 1-3 shows an example of a coating thickness distribution across the coating cross section on a flat plate for two different pulse energies. The coating thickness was measured on the fracture surface with the help of a 3D laser scanning microscope (LSM) of type Keyence VK 9700. The widely distributed coating thickness, which showed a maximum in the region of the target normal, could be attributed to the quasi-pointwise particle emission from the target. Furthermore, the influence of the pulse energy on the ablation direction is made evident by the different slopes of the two curves. In the test setup used in this work, the spheres to be coated are located on a circular area of diameter 20 mm at a distance of 40 mm from the target. They exhibit an ablation angle of 30° in with respect to the target normal, achieving the maximum coating rate with largely homogeneous coating of the moving spheres.

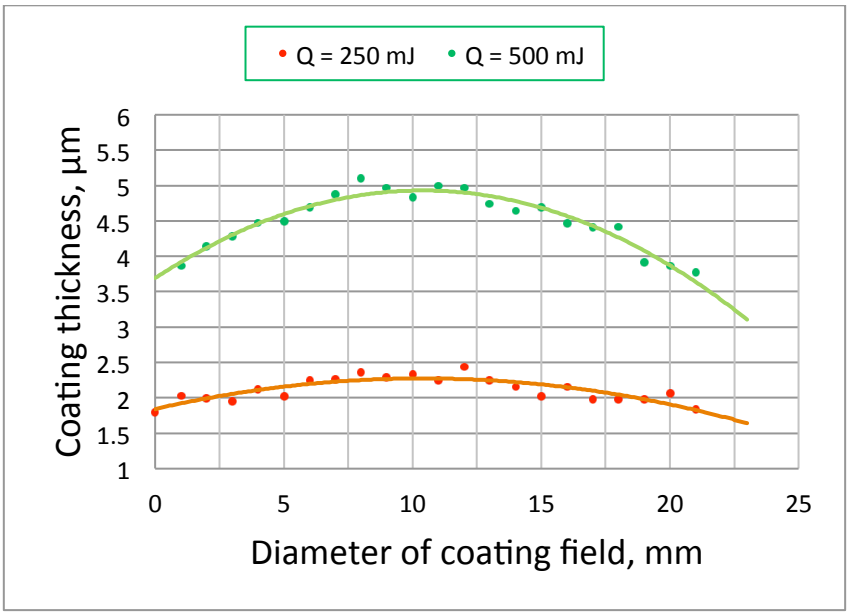

Figure 1-3: Change in coating thickness over the area of a planar substrate as a function of pulse energy for a spacing of 40 mm between target and substrate

1.3.5 Coating Temperature

The temperature of the samples to be coated was adjusted by means of a 3 kW diode laser and could be varied freely over a wide range. With silver, a common coating material for mirrors, the absorption of this laser radiation of wavelength 808 nm is limited to about 3% [36]. In contrast, SiC absorbs the laser radiation with an efficiency of greater than 99% [37]. For B_4C, a similarly high absorption can be expected. Unlike the noble metal silver, the chemical composition of PLD-SiC and PLD-B_4C, respectively, does not necessarily equal the stoichiometric composition of the target and is a function primarily of the vacuum conditions and the coating temperature. The microstructure of the coatings depends on these parameters as well. It must be assumed that the individual atoms and ions of SiC in the plasma will be deposited independently of each other in case of an unheated substrate. Only starting at a specific substrate temperature it can be expected that chemically bonded SiC with an amorphous structure and possibly free Si and/or C will form. According to the literature, the crystallization temperature of SiC is approximately 800 °C [38]. In fact, the crystallization temperature may vary as a function of the deposition parameters, such as the substrate material and the deposition rate, making it possible for a wide range of crystallization temperatures to be yielded with the PLD technology. In addition, the particle energy and the coating time also affect the coating microstructure

(Figure 1-4 [39]). These parameters can be varied appropriately to obtain the desired crystallite size and shape.

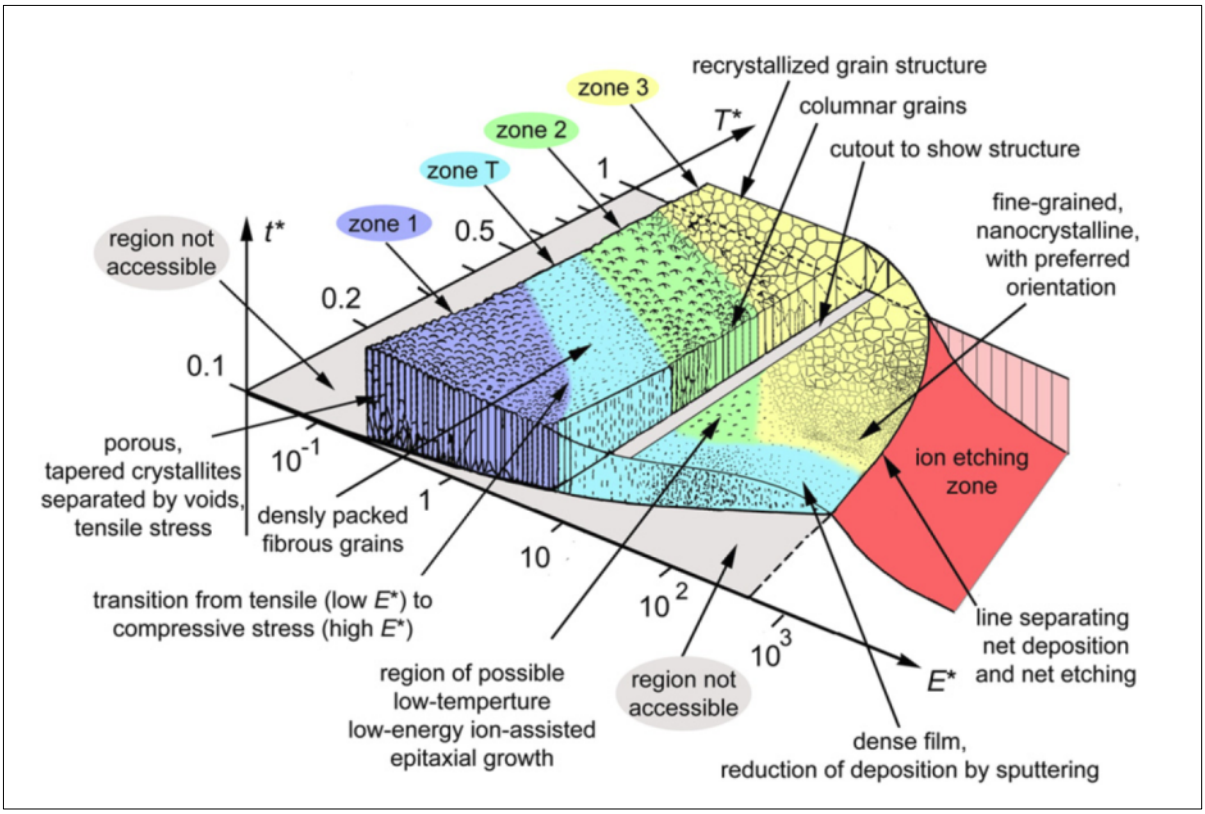

Figure 1-4: Structure zone diagram [39]. The coating microstructure proved to be dependent on the homologous substrate temperature, the normalized particle energy, and the normalized coating thickness. At a very high particle energy, instead of coating, removal of the substrate surface occurred ("ion etching").

The particles coated within the scope of this work had to be moved constantly during the coating process, which took place in a vacuum, in order for a uniform coating structure to be achieved over the entire particle surface. This made temperature measurement even more difficult. The only possibility was via contactless measurement through a window in the vacuum chamber. In this work, the measurement was carried out using an infrared camera, which was installed at a distance to the object of about 40 cm. With a resolution of 1280 x 960 pixels and an image field of 160 x 120 mm², each particle was represented only by 4 x 4 pixels (Figure 1-5). Movement of the particles during measurement resulted in large uncertainties, which, however, could be reduced through measurement of the temperature right after the spheres came to a standstill.

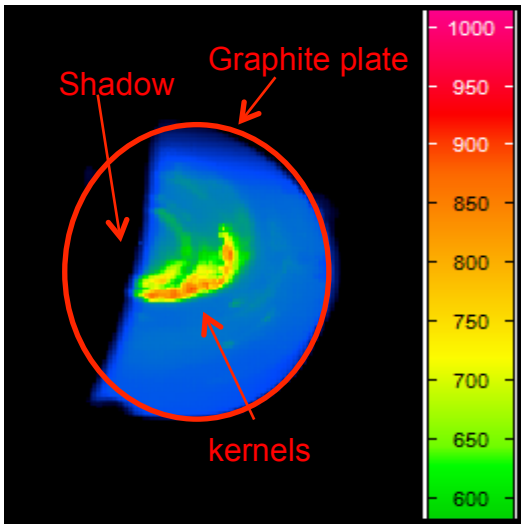

Figure 1-5: Thermogram of heated spheres at standstill, Tmax = 980 °C

1.3.6 Coating Atmosphere

The PLD process was performed in a vacuum, primarily to ensure unimpeded spreading of the target components and avoidance of interactions with other elements between the target and the substrate. In the vacuum chamber used, a high vacuum of 10^{-4} mbar was generated. This reduced the number of species from 10^{19} cm^{-3} at normal pressure to 10^{12} cm^{-3} under vacuum conditions. Both the melting and boiling temperatures of elements and compounds depend on the pressure of the surrounding atmosphere. If crystalline SiC is deposited onto a silver coating at the necessary deposition temperature of > 800 °C, it must be ensured that the temperature-dependent partial pressure of silver [40] does not get too high (Figure 1-6). To accomplish this, the pressure in the vacuum chamber can be increased accordingly. In the experiment, a pressure of 2.5 x 10^{-1} mbar was hence chosen when crystalline SiC was to be deposited onto silver. However, this change in pressure immediately resulted in an increase in particle density to approx. 10^{15} cm-³ and hence a reduction in the mean free path from 10 m at 10^{-4} mbar to 10 mm at 10^{-1} mbar. Not only did the probability of collisions increase, but the probability of contamination of the coating by incorporation of oxygen and nitrogen as main components of the air also increased. Purging the chamber with an inert gas (Ar in this case) can counteract the chemical reaction, but a change in the stoichiometry of the coating composition can then be expected. The reason for this is the fact that the cross section of argon atoms is nearly three times that of oxygen or nitrogen atoms, which increases the probability of collision of the gas atoms with the relatively large Si ions.

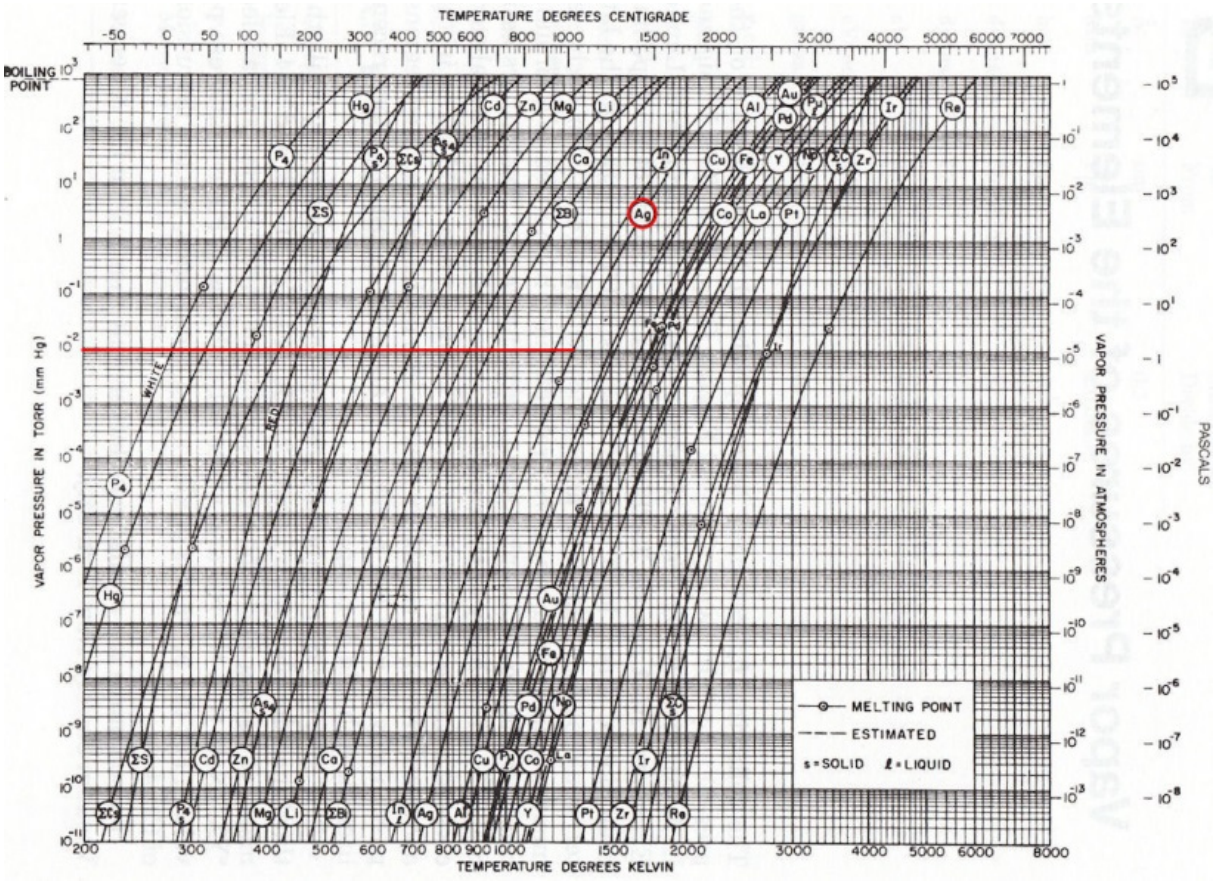

Figure 1-6: Dependence of vapor pressure on temperature for selected elements [40]

1.4 Experimental

1.4.1 Experimental Setup

For generation of silver and SiC coatings on the spheres, a PLD test system using an excimer laser unit for ablation of the coating material was installed. A Coherent LPX Pro 305i excimer laser with a wavelength of 248 nm, a pulse duration of 25 ns, and a pulse repetition frequency of 40 Hz was used. The wavelength of the laser pulses in the UV range ensured the ablation of material required in the PLD process by explosive evaporation with a very small heat-affected zone. The laser had a maximum pulse energy of 1.1 J, yielding a laser fluence of 20 J/cm² for a focused laser beam cross-sectional area of about 5 mm^2. According to Reitano et al. [32], the ablation threshold for SiC is 1.1 J/cm².

A diode laser beam with a wavelength of 808 nm was also directed at the moving spheres to heat them up to the required substrate temperature. The wavelength of 808 nm and the

selected laser power ensured that the energy input by the diode laser did not reach the ablation threshold of SiC.

A high-vacuum chamber with a capacity of 0.03 m³ housed the coating equipment as the receiver for the PLD process. Unless otherwise stated, the tests were conducted in a high vacuum of $< 9*10^{-4}$ mbar. A total of four optical windows were provided, one for transmission of the excimer laser radiation to the target, one for transmission of the diode laser radiation to the spheres to heat them up, one for recording of the sample temperature via the infrared camera, and one enabling observation of the process. The windows were made of quartz glass or zinc selenide glass according to the wavelengths to the transmitted. Through-holes were provided for chamber evacuation, power supply to and cooling of motors, and transmission of rotation to the target holder. A schematic diagram of the working chamber showing the test setup is given in Figure 1-7.

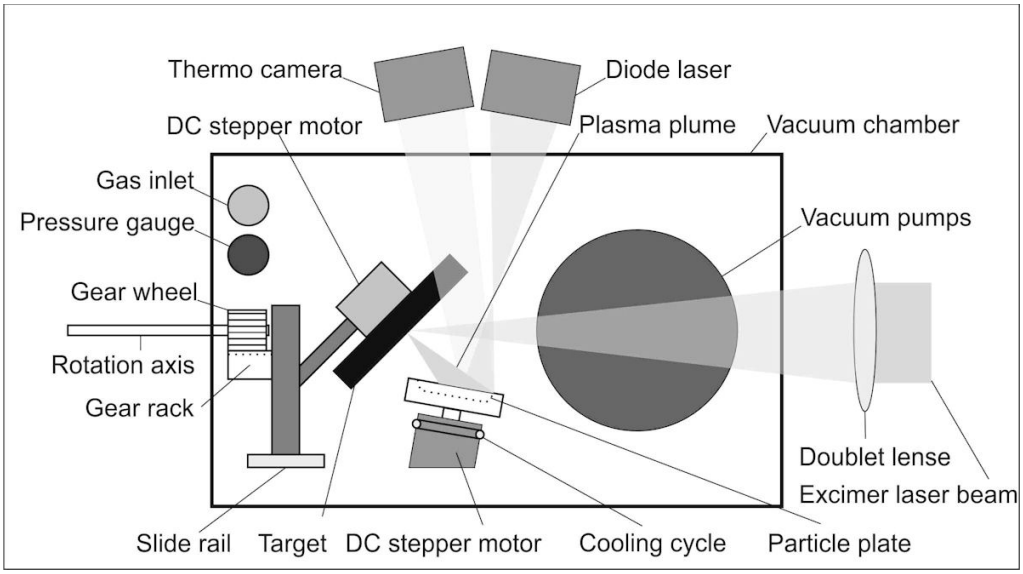

Figure 1-7: Schematic diagram of working chamber test setup

A holder enabling fixation as well as translational and rotational movement of the target relative to the excimer laser beam via a stepper motor was installed in the vacuum chamber. Uniform surface removal of the target at an angle of 30° to 60° to the beam axis was achieved by sliding of the unit along a rail. With control of the rotation with variable speed and simultaneous superimposition of the constant rotational speed of the vacuum-grade stepper motor (to 10^{-4} mbar) from Phytron, the laser beam described a spiral path on the surface of the target, enabling uniform removal of the target surface at a constant laser pulse frequency.

1.4.2 Development of Experimental Equipment for PLD Coating of Spherical Substrates

Apart from suitable laser and operating parameters, uniform and complete rotation of the spherical substrates (“kernels”) during the coating process is crucial for a good coating quality. Vacuum-grade, temperature-resistant, durable components that allow for continuous coating of the spheres without any shadowing of the plasma plume are required to ensure a high, uniform deposition rate. In the CVD (chemical vapor deposition) method conventionally used for coating of spherical nuclear fuel, uniform coating is achieved through a fluidized bed generated by a gas flow [29][30][31]. Because a vacuum precludes the use of flowing media, an alternative method had to be developed to achieve uniform kernel motion. The stated requirements were incorporated into a construction for moving the spheres on a stepped plate that was aligned parallel to the target and ensured conveyance of the spheres at a constant distance to the target through use of a pneumatically controlled lifting device.

Initial testing of the device shown in Figure 1-8 for coating the spherical particles was performed. Utilizing their elasticity (Young’s modulus of the substrate material ZrO_2 = approx. 200 GPa [33]) and inertia, the spheres moved up the profiled conveyor plate raised at a lifting frequency of about 1 Hz, rolled down the sides, and were again accelerated to the top of the profiled plate in a renewed cycle. The orientation of the profiled plate at an angle of 45° to the base plate and hence parallel to the target enabled the spheres to be heated via a second laser beam (diode laser), which was transmitted into the chamber through the window above it (Figure 1-7). The setup using a diode laser for substrate heating had been successfully used for coating of planar substrates before [49]. The spacing between the target and the substrate was 45 mm, similar to that used for coating of planar substrates. The spheres were moved rhythmically, rotated about their central axes, and continuously coated.

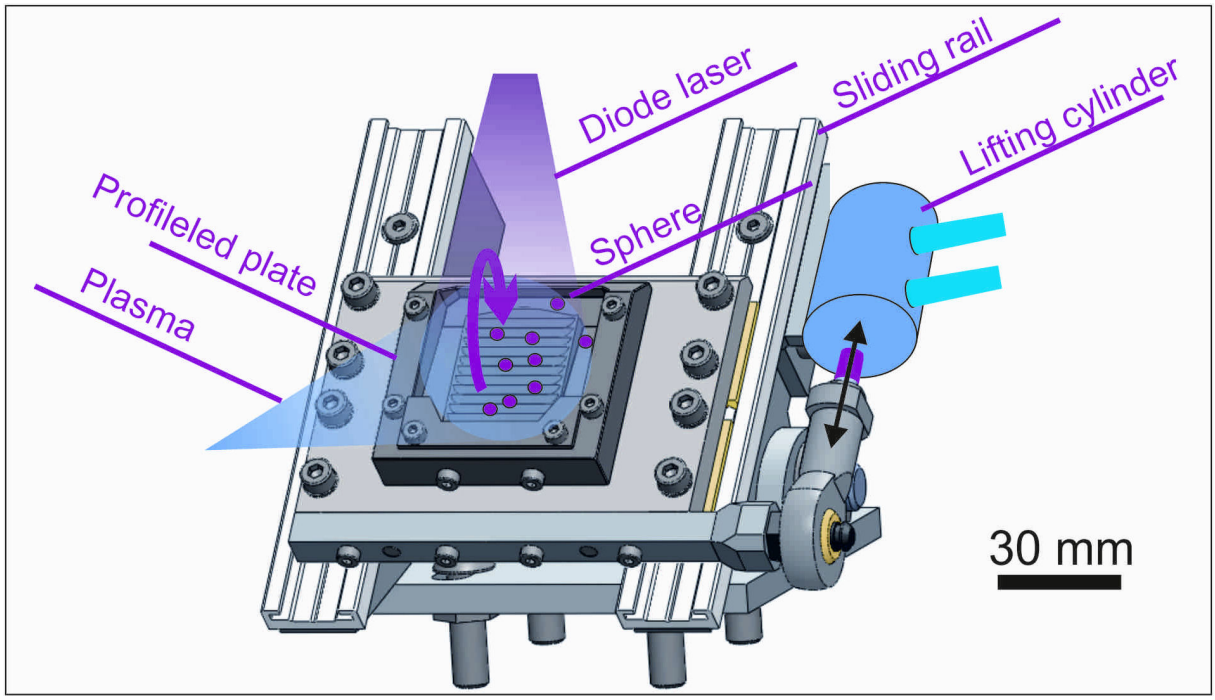

Figure 1-8: Sphere-conveying device 1

This holder proved to be suitable for generating thin coatings of thickness on the order of a micrometer (coating duration: ≤ 30 min). In contrast, for longer processing times for generating thicker coatings, the lifting cylinder frequently failed due to increased friction of the plungers in the lifting cylinders caused by thermal expansion and contamination of the plungers during the coating process. Even when the moving parts were covered as a protection from the particle flux, the problem persisted. To address these findings, an alternative particle-moving device was developed (shown in Figure 1-9). The particles were in a graphite crucible oriented at a 10° angle, whereby the plate diameter of 10 mm corresponded to the diameter of the diode laser beam in this plane. The graphite plate was secured pointwise to an aluminum adapter, which was rotated uniformly at 25 rounds per minute by a water-cooled motor. The motor was the same as the one used for target rotation and exhibited stable operation during the coating tests.

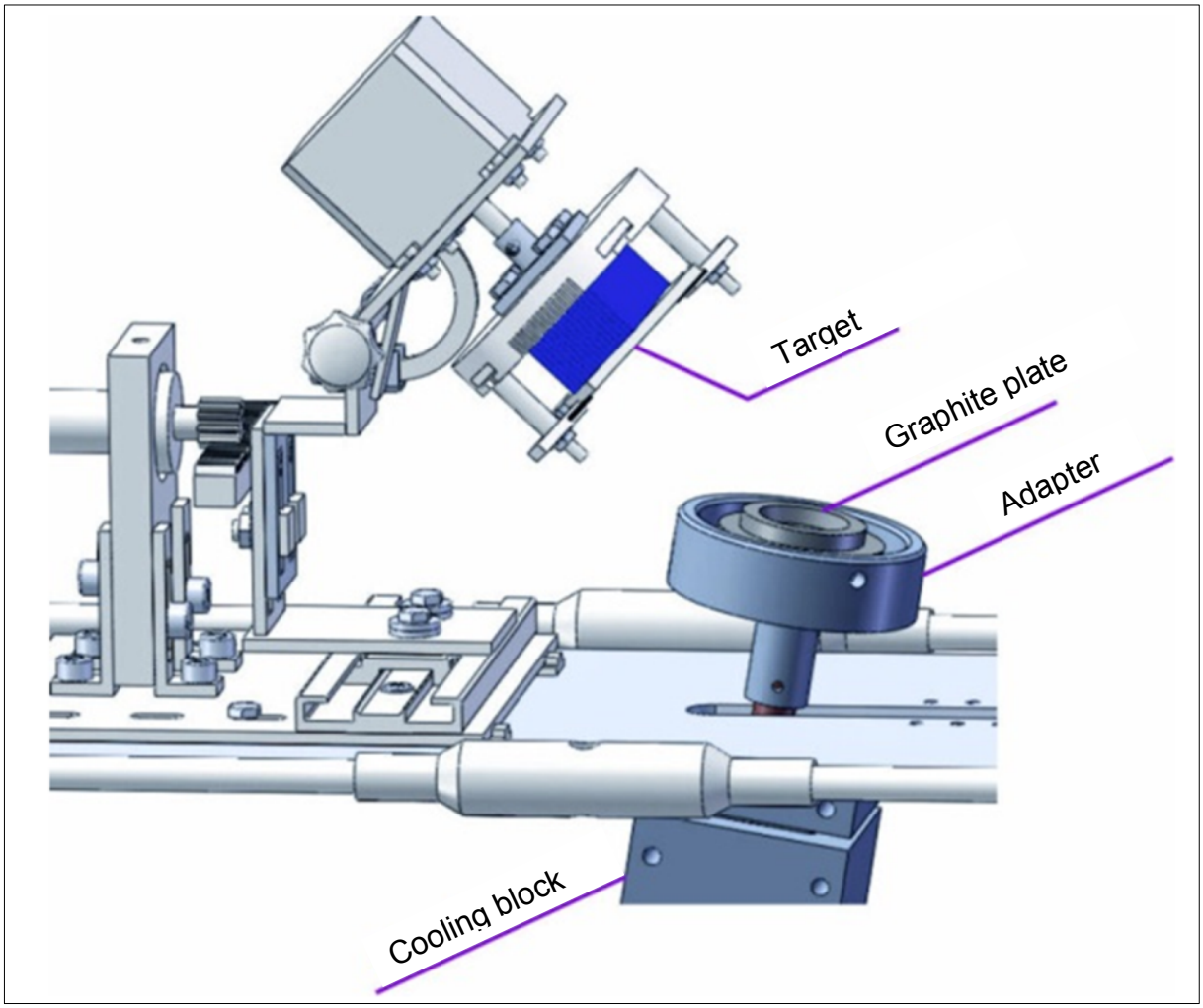

Figure 1-9: Modified holder for sphere coating

Comparison of a (planar) circular area and the surface of a sphere through the equation $\frac{\pi}{4}d^2 = k \cdot \pi d^2$ yielded a relationship k = 1/4, meaning that the deposition rate of spheres was expected to be only one-fourth of that of planar substrates. In the case of planar substrates, the coating rate was determined in the tests to be approximately 3 nm/s. Until a coating thickness of 10 µm on the surface of the sphere was reached (CVD coating was about 35 µm [34]), the deposition rate decreased continuously due to the accompanying decrease in the transmission of the coupling window for the excimer laser. Measurements yielded an energy acting on the target Q_t of approx. 72% of the originally determined laser pulse energy Q_0. The reason for this was the secondary coating of the coupling window angled at 45° to the coating axis, although this coating was minimized through insertion of a screen and placement as far from the target as possible (distance: 400 mm). The time required to reach a specific coating thickness was empirically determined as:

$$t = v_{plate} \cdot s : T \quad (1.1)$$

where t was the coating time, v_{plate} the deposition rate on planar substrates, s the coating thickness, and T the transmission of the window. This approximation yielded a processing time of 5.1 hours for a coating thickness of 10 µm, which was confirmed experimentally. However, only the modified test setup shown in Figure 1-9 was suitable for conducting these lengthy coating tests.

1.4.3 Materials Used

The coating tests were performed on alumina (Al_2O_3) and zirconia (ZrO_2) particles approx. 500 µm in diameter. According to the literature, these are the usual substrate materials used for investigating processes of diffusion of silver through SiC barrier coatings and served as a benchmark for comparison of the results. In addition, this work used optimized coating technology on spherical ZrO_2 substrates that were previously coated in a CVD process with a buffer layer and a pyrolytically deposited carbon coating at the University of Manchester to exhibit similar properties to those of TRISO particles.

As coating materials, i.e., targets, silver, silicon carbide (SiC), and boron carbide (B_4C) were used. The main properties of the substrate and target materials are summarized in Table 1 and Table 2.

Table 1 Physical properties of the target materials

	Silver *	SiC Target **
Density, gcm^{-3}	10.5	3.16
Melting temperature, °C	961.9	> 2300
Coefficient of thermal expansion at 1000 °C, 10^{-6} K^{-1}	19.1 (20 °C)	5.2
Thermal conductivity, $W(mK)^{-1}$	429	125
Young's modulus at 20 °C, GPa	82.7	420
Poisson's ratio	0.367	0.17
Purity, %	99.99	99.9

*) Sputter target Ag Goodfellow GmbH, **) EKasic Fplus ESK Ceramics,

Table 2 Physical properties of the substrate materials

	Spherical substrate
	ZrO_2
Density, gcm^{-3}	6.0
Melting temperature, °C	
Coefficient of thermal expansion at 1000 °C, 10^{-6} K^{-1}	10.8
Thermal conductivity, $W(mK)^{-1}$	2
Young's modulus at 20 °C, GPa	210
Poisson's ratio	
Surface roughness Ra, µm	0.01

*) Tosoh Corporation,

Due to the different methods used to prepare them, the individual substrates exhibited different surface properties. The surface roughness is a significant factor in coatings because it determines whether the coating adheres to the substrate by (chemical or physical) adhesion only or additionally by mechanical anchoring [35]. The linear roughness R_a measurements listed in Table 2 fluctuated greatly among the spherical substrates. Micrographs of the substrate surfaces are shown in Figure 1-10 to Figure 1-12.

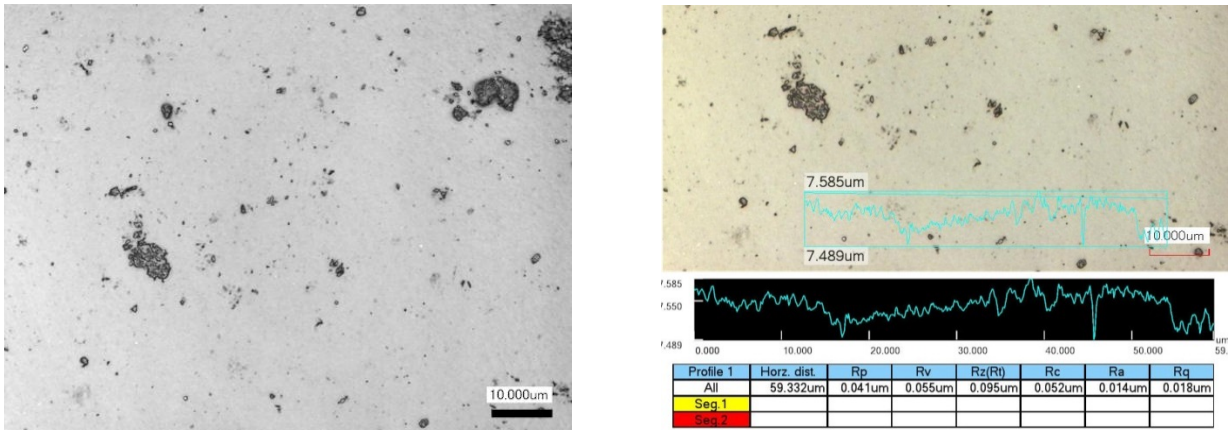

Figure 1-10: LSM surface and roughness of zirconia spheres (Ra = 14 nm)

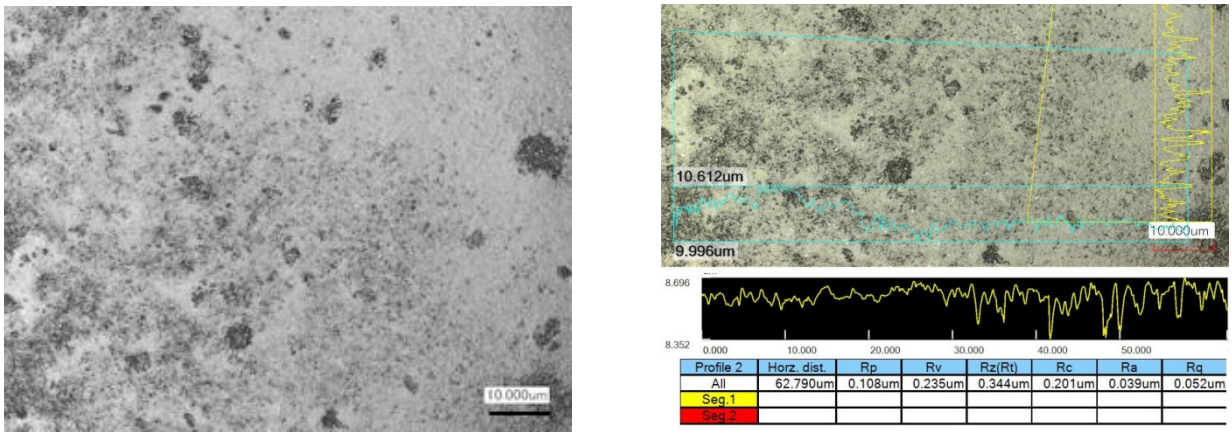

Profile 2	Horz. dist.	Rp	Rv	Rz(Rt)	Rc	Ra	Rq
All	62.790um	0.108um	0.235um	0.344um	0.201um	0.039um	0.052um
Seg.1							
Seg.2							

Figure 1-11: LSM surface and roughness of alumina spheres (Ra = 40 nm)

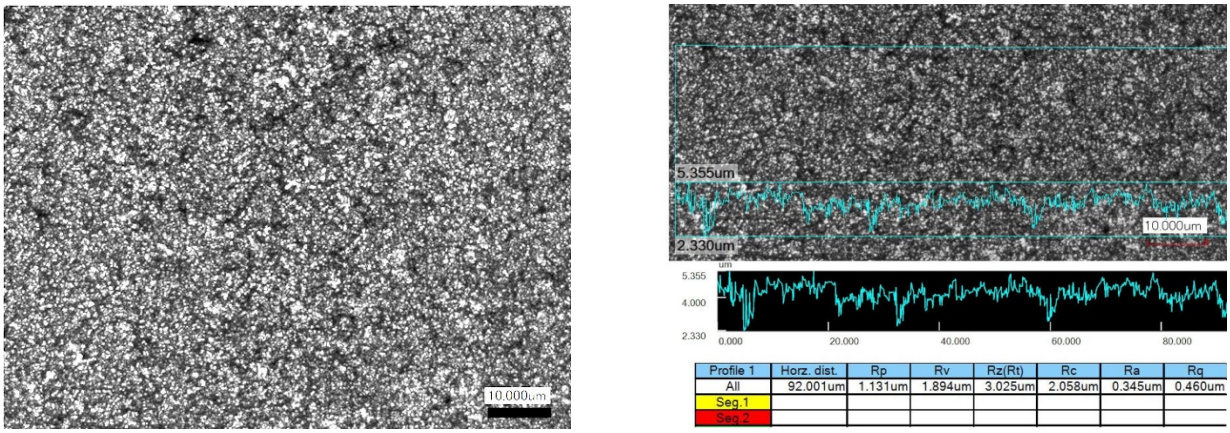

Profile 1	Horz. dist.	Rp	Rv	Rz(Rt)	Rc	Ra	Rq
All	92.001um	1.131um	1.894um	3.025um	2.058um	0.345um	0.460um
Seg.1							
Seg.2							

Figure 1-12: LSM surface and roughness of carbon-coated ZrO_2 spheres (Ra = 345 nm)

1.5 Results

1.5.1 Coating of ZrO_2 Particles With Silver

Coating with silver was performed at a pulse energy of 60 mJ, a pulse repetition frequency of 40 Hz, a coating time ranging from 5 to 15 min at room temperature, and a chamber pressure of 10^{-4} mbar. The resultant coating thickness was between 50 nm and 300 nm.

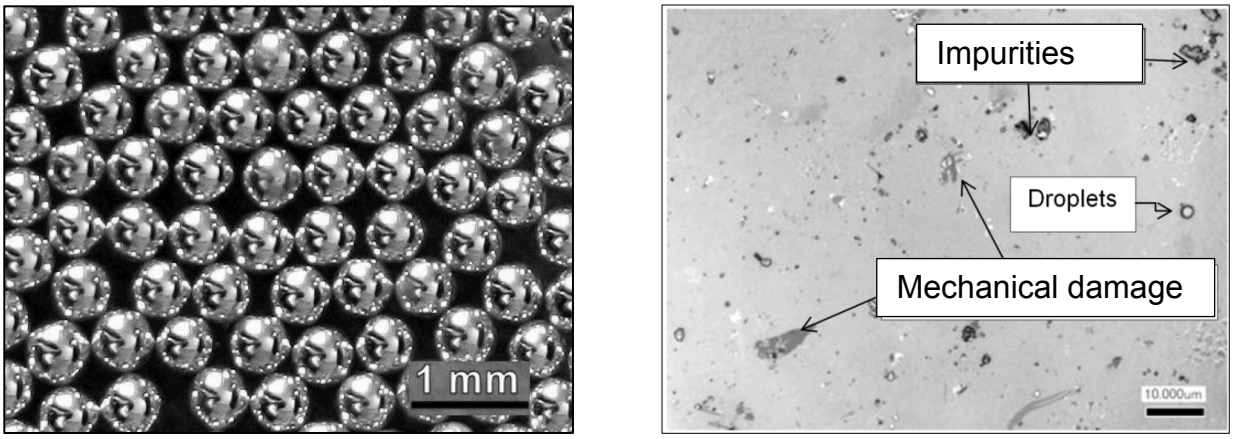

Figure 1-13: Photo of silver-coated spheres (left) and LSM micrograph of surface of silver coating (right) with typical impurities and mechanical damage

A photograph of coated particles and a LSM micrograph of the surface are shown in Figure 1-13. The micrograph shows typical impurities such as droplets, mechanical damage, and adhering contaminants. The number of droplets was found to increase with increasing pulse energy.

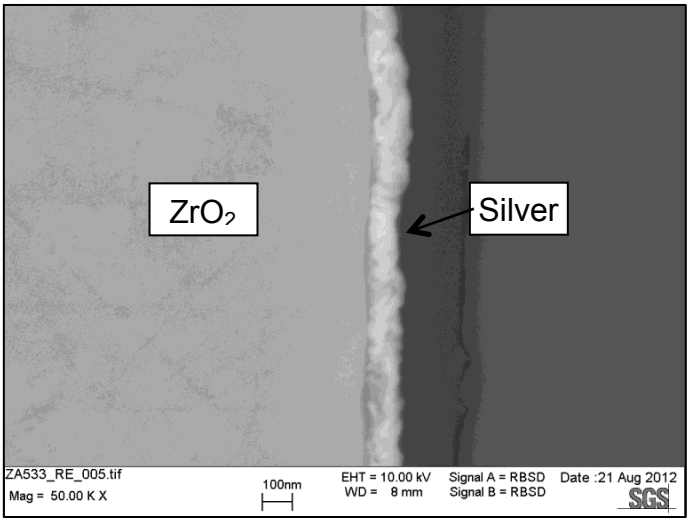

Figure 1-14: Cross section through a silver coating (SEM micrograph)

Figure 1-14 shows an SEM micrograph of a polished cross section through an approximately 100-nm-thick silver coating. The coating shows none of the pores or blowholes that would be expected with accumulation of particulates or droplets due to shadowing effects. The coating is homogeneous and adheres strongly to the substrate. The shadowing that can be observed in Figure 1-14 is presumably due to preparation

artifacts. With these findings, it could be shown that silver, as an indicator for diffusion processes, could also easily be deposited onto spherical substrates.

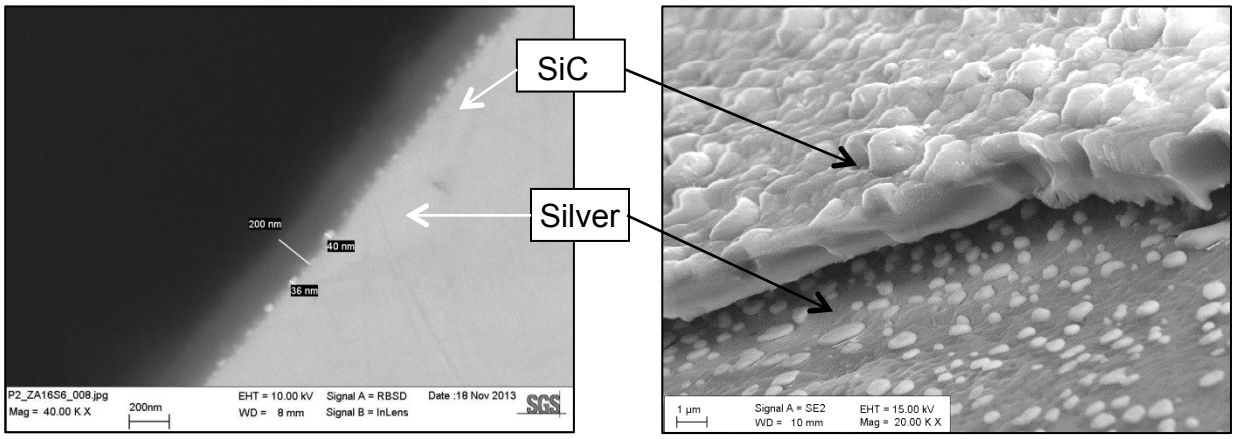

Figure 1-15: SEM micrographs of a UMAN polished cross section (left) and a fracture surface (right) of an approx. 50-nm-thick silver coating after SiC coating at 1000 °C with a chamber pressure of 10^{-1} mbar

Figure 1-15 shows a silver coating with an original thickness of about 50 nm after subsequent application of an additional SiC coating deposited at 1000 °C and a chamber pressure of 10^{-1} mbar. It can be seen that silver melted, formed fine beads, and solidified during deposition. No silver deposits can be detected in the SiC coating.

1.5.1.1 Coating of ZrO_2 Particles with SiC on Silver at Room Temperature

Coating with SiC on Ag was performed in the first step at room temperature in a high vacuum. With a pulse energy of 350 mJ and a pulse frequency of 40 Hz, it took about 58 min to generate spherical coatings comparable to those on the planar substrates (Figure 1-16).

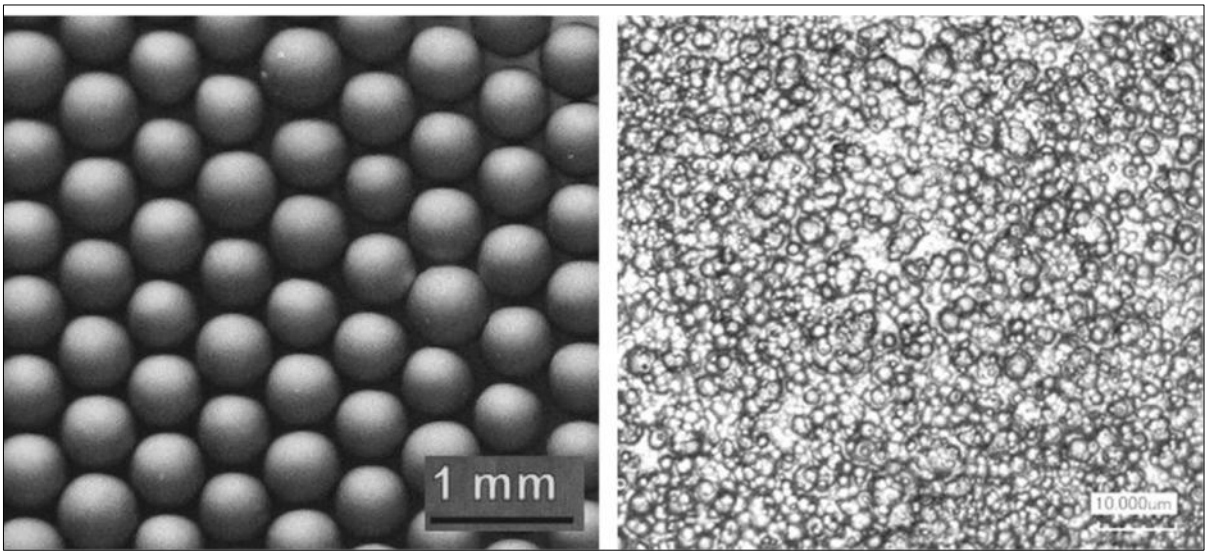

Figure 1-16: Coated ZrO_2 spheres mit 4-µm-thick SiC coatings on intermediate silver coatings: photograph (left) and LSM micrograph of specimen surface (right)

The thickness of this coating was approximately 4 µm. Crack-free and well-adhering coatings of thickness greater than 7 µm were also obtained. Thicker SiC coatings were not investigated. The surface structure (Figure 1-16) results neither from droplets nor from the roughness of the ZrO_2/Ag surface. The coatings deposited at room temperature exhibit inhomogeneities in the form of conical structures (Figure 1-17), which presumably lead to this surface structure. At higher deposition temperatures of between 350 °C and 600 °C, they were not observed to the same extent.

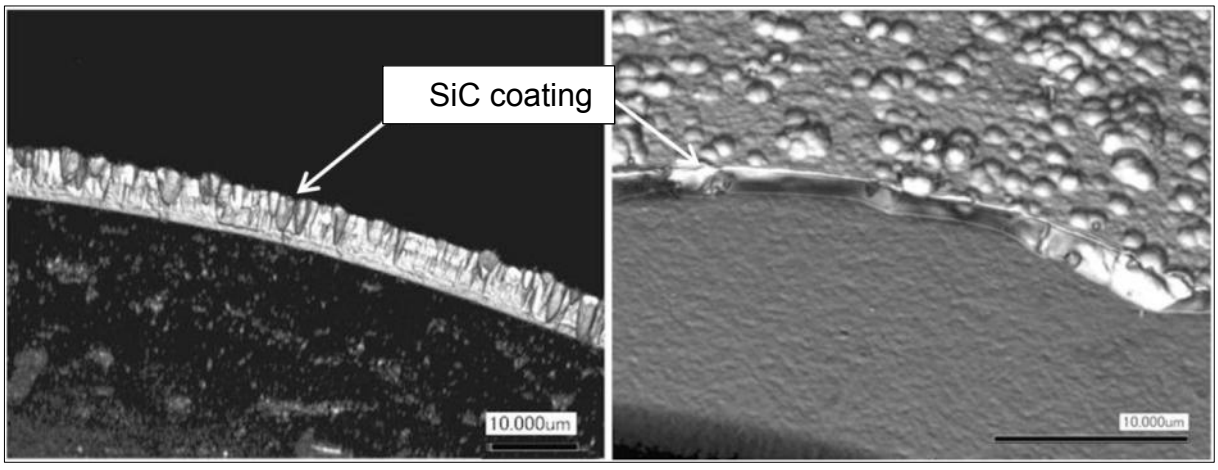

Figure 1-17: LSM micrographs of the fracture surface of an SiC coating at room temperature (left) and at > 350 °C (right)

The micrograph on the left in Figure 1-17 shows the fracture surface of an SiC shell, clearly showing these conical structures. The right micrograph, in contrast, shows the typical, glass-like fracture surface of amorphous SiC coatings, as is known from coating of planar substrates ([41]). Of all spheres coated under these conditions, 97% exhibited dense interfaces between the ZrO_2 kernel, the silver coating, and the SiC coating.

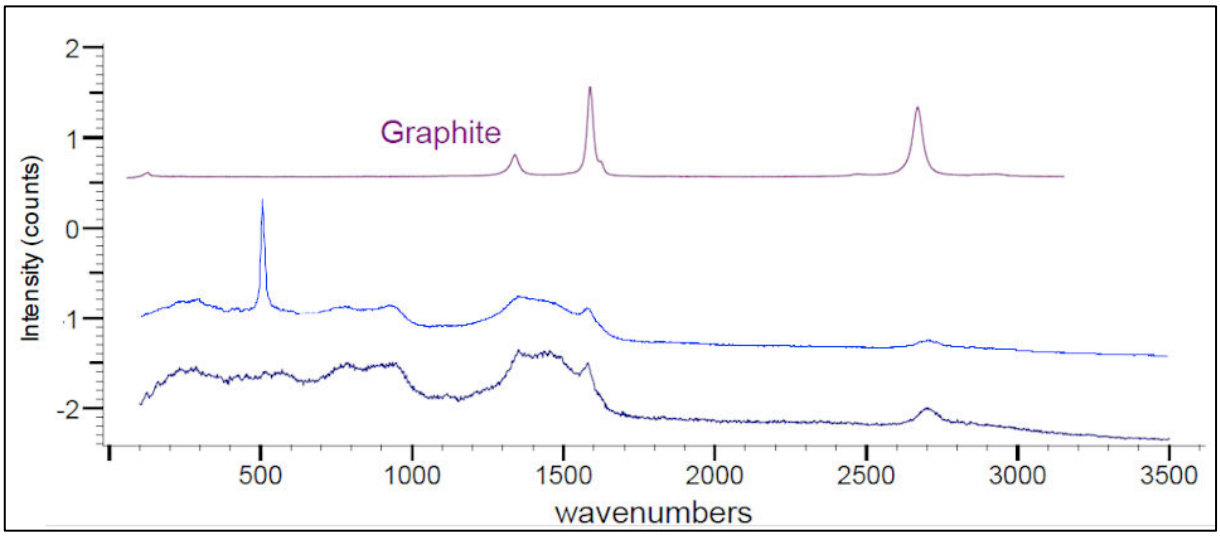

Figure 1-18: RAMAN spectra for a SiC coating deposited at room temperature

RAMAN spectra of these coatings, which were deposited at a temperature of less than 300 °C, are given inFigure 1-18. The two lower spectra represent typical measurement results, whereby the narrow peak at a wave number of 520 can clearly be assigned to silicon. Additional peaks in the regions corresponding to graphite (exemplified by the upper curve) point to amorphous carbon due to their broadness and low intensities. SiC was not found in any of its modifications. Deposition of SiC at substrate temperatures of less than 300 °C was shown to lead to the existence of the separate elements Si and C and not to the chemical compound SiC.

1.5.1.2 Coating With SiC on Silver in Temperature Range from 350 °C to 800 °C

For deposition of an approx. 5-µm-thick SiC coating onto silver at a temperature ranging from above 350 °C to approx. 800 °C, the extent of spalling of the layer was seen to coincide with the increase in temperature.

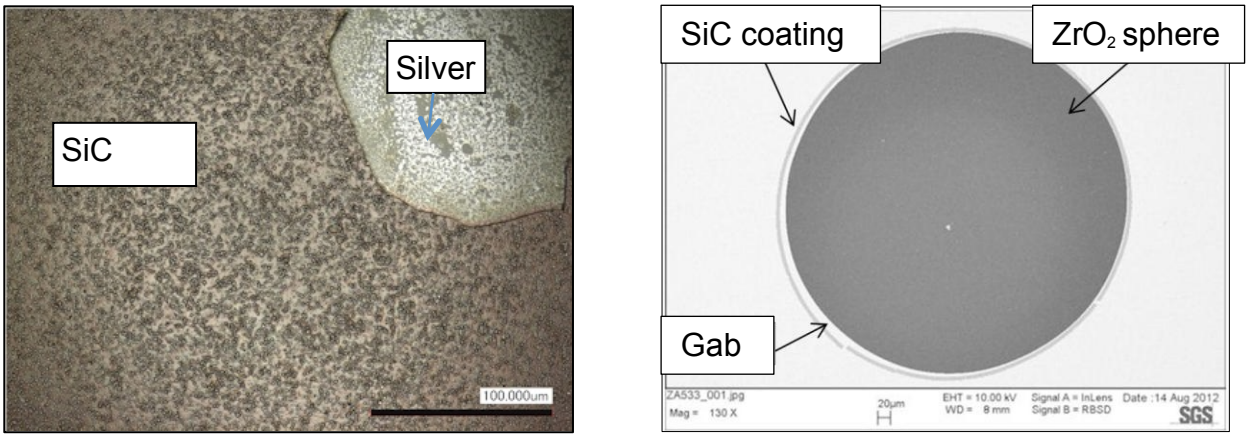

Figure 1-19: LSM micrograph of an SiC coating deposited onto silver at a temperature of about 700 °C in an argon atmosphere at 2.5 x 10^{-1} mbar, showing the typical spalling (left), and LM image of a cross section through an SiC coating under compressive stress with partial stress relief through crack formation (right)

Figure 1-19 shows an example of a slab that spelled off at a coating temperature of 700 °C due to a closed, web-like crack structure. The cross section to the right clearly shows that the SiC is mostly detached from the surface of the sphere. From the literature, it is known that for coating processes such as PLD with energetic particles, compressive stresses arise in the coating [42] [43]. A relationship between the substrate temperature and the increase in compressive stresses in the coating was found, with the slope starting off low at T_S = 600 °C and increasing steadily starting at a temperature of 800 °C. Zehnder et al. attributed this to densification of the crystalline coating structure and hence to a more pronounced effect of particles of high kinetic energy that became implanted in the coating [44]. The observation of stress-induced cracking with increasing coating temperature in the range between 350 °C and 800 °C was confirmed in the tests performed in this study.

X-ray photon spectroscopic investigations of the SiC coatings deposited at a temperature of greater than 350 °C yielded information about the coating compositions, as shown in Figure 20 for planar specimens.

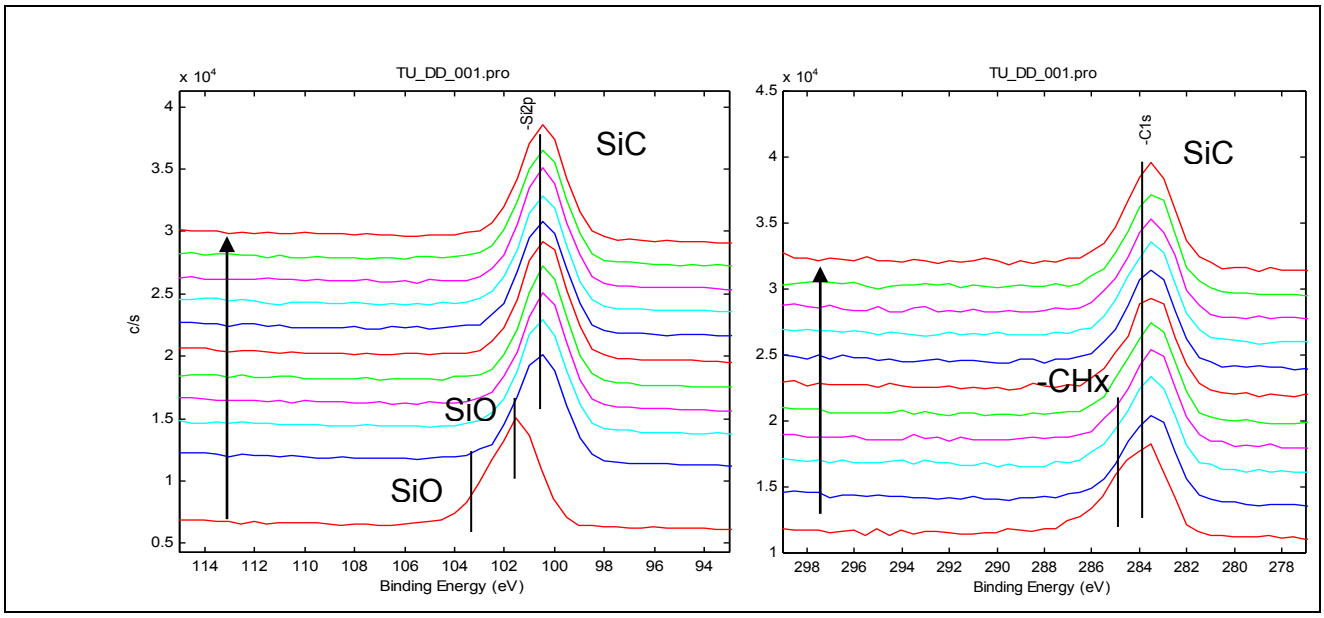

Figure 1-20: Results of XPS investigations of SiC coatings deposited at a temperature of greater than 350 °C for the region from the surface down to a depth of 50 nm

Figure 1-20 illustrates the binding energies measured in the coatings. The ordinate indicates the sequence of sputtering cycles, with the maximum penetration depth being 50 nm. No changes were found at greater depths (> 10 nm). Primarily via the first two spectra, a shift in both the Si2p peak and the C1s peak, both of which were caused by near-surface reactions with reaction products SiO_2, SiO_x, and CH_x, was recorded. In contrast, starting at a depth of 10 nm, clear Si2p and C1s peaks were formed, providing evidence of a nearly stoichiometric SiC coating. Crystalline components of the coatings deposited at temperatures below 800 °C were precluded due to the crystallization temperature of ≥ 800 °C.

1.5.2 Coating of Silver with SiC in Temperature Range From 800 °C to 1000°C

Submicrometer-to-micrometer-thick SiC coatings on silver could not be deposited without cracking at a coating temperature of > 800 °C and a chamber pressure of 2.5 x 10^{-1} mbar. Tests performed at low temperatures (ca. 350 °C) for the first 15%–85% of the coating time and at higher temperatures for the remaining time (in a fine vacuum in both cases) also led to cracking of the coating. Tests performed at low temperatures (ca. 350 °C) for the first 15%–85% of the coating time in a high vacuum (4 x 10^{-4} mbar) and at higher temperatures for the remaining time in a fine vacuum (2.5 x 10^{-1} mbar) yielded significantly different results.

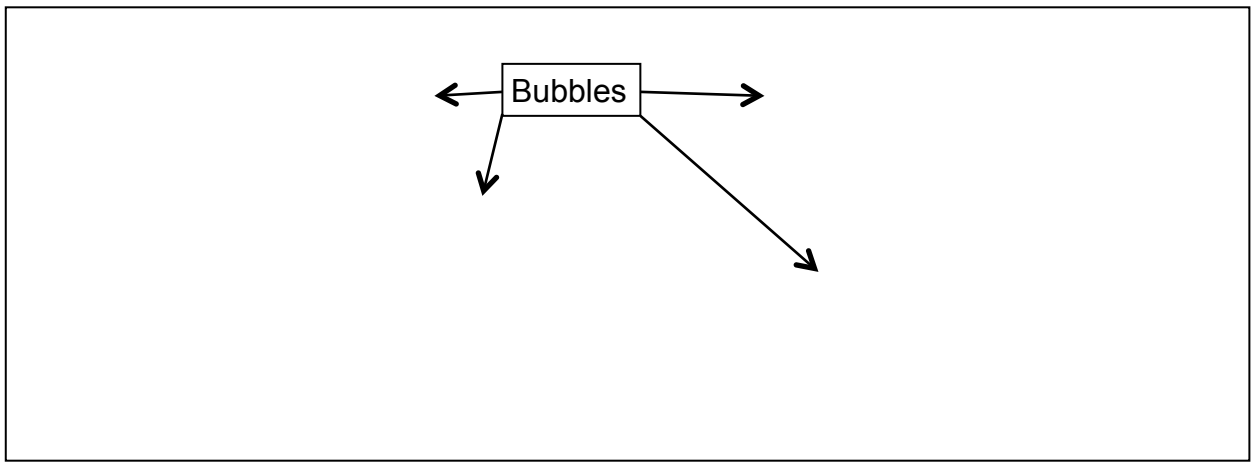

Figure 1-21: LSM micrographs of SiC coatings on silver with t1 = 10 min, T1 = 350 °C, and p1 = 10^{-4} mbar; and t2 = 2 min, T2 = 800 °C, and p2 = 10^{-1} mbar

Figure 1-21 shows a typical SiC coating of thickness ≤ 1 µm produced in two different pressure (high vacuum or fine vacuum) and temperature (< 800 °C or > 800 °C) regimes. Unlike the coatings deposited in a fine vacuum at comparable temperatures, these coatings did not show, or rarely showed, cracking. The coatings exhibited discrete buckled regions but otherwise exhibited good adhesion. It was not possible in this study to determine any influencing factors for the manifestation of the humps. For coating temperatures of about 1000 °C, cracks arose primarily at the hump boundaries, sometimes causing the buckled surfaces to detach, and were intertwined. The extent to which the coating leads to recrystallization of the underlying amorphous coating deposited at temperatures above 800 °C is not known.

In none of the coatings produced under the conditions described above could a crystalline phase be detected by XRD. EDX analysis of the coatings supplies possible reasons for this. Table 3 lists the chemical compositions of the coatings deposited at various temperatures and pressures.

Table 3 Chemical compositions of coatings deposited at various temperatures

Pressure, mbar	10^{-4}	10^{-3}	10^{-4}, 10 min 10^{-1}, 5 min
Temperature, °C	25	800	900
Element, atom %			
C K	26.93	62.94	75
O K	47.93	11.42	25
Si K	25.13	25.64	12.5
Si/C	**0.93**	**0.41**	**0.16**

The oxygen content of the coating is strikingly high and fluctuates strongly with changes in chamber pressure and temperature. The detection of oxygen can in principle be traced back to the significantly higher excitation depth for this light element. The silicon-to-carbon ratio decreases strongly with increasing chamber pressure and temperature. Under these circumstances, formation of a stoichiometric SiC phase is unlikely.

With knowledge of the coating composition, more tests were performed to determine the extent to which multiple purging of the chamber with argon to minimize the residual oxygen content changed the coating stoichiometry. In this test series, the ratio between low-temperature coating (at 350 °C) and high-temperature coating (at 800 °C) was changed from 5:1 (Figure 1-21) to 2.67:1 to recrystallize the amorphous structure. Coatings were deposited onto Al_2O_3 particles with the aim of determining whether or not the effect of different particle expansion behavior could help explain the occurrence of buckling.

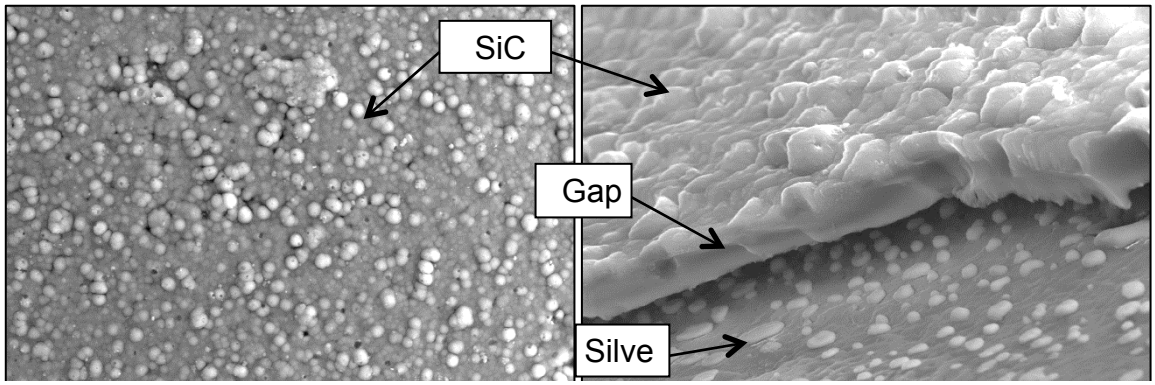

Figure 1-22: SEM micrographs (JRC-IET, Petten) of the surface of the SiC coating (left) and a cross section through the fracture surface of the coating on silver (right) for a coating thickness of 2 µm and Ra = 100 nm, with t1 = 40 min, T1 = 350 °C, and p1 = 10^{-4} mbar; and t2 = 15 min, T2 = 800 °C, and p2 = 10^{-1} mbar

Figure 1-22 presents coating surface micrographs. The coating surface appears to be homogeneous, highly densified, and free of cracks (cf. Figure 1-19 and Figure 1-21). Mechanical loading of the SiC coating leads to coating fracture and reveals the low adhesion to the substrate (right). The intermediate coating and the substrate exist side by side without being mechanically anchored or joined by adhesion or chemical bonding. In contrast to coating deposition onto ZrO_2 kernels, in this case, no buckling occurred.

Table 4 **Chemical compositions of the SiC coatings deposited onto silver after three argon purging cycles in the vacuum chamber for a coating thickness of 2 µm with t1 = 40 min, T1 = 350 °C, and p2 = 10^{-4} mbar; and t2 = 15 min, T2 = 800 °C, and p2 = 10^{-1} mbar**

	C	O	Si	Si/C
Atom %	40.16	18.73	41.11	**1.02**

Table 4 shows the results of EDX analysis. Increasing the purity of the working atmosphere resulted in a coating with a nearly stoichiometric ratio of Si:C of 1.02. Despite the coating temperature of 800 °C and the stoichiometric Si:C ratio, no crystalline SiC phases could be detected for a coating thickness of 2 µm.

1.5.3 Coating of Carbon-Covered ZrO_2 Particles with Silver and SiC

The extent to which the results of the silver-SiC coating systems deposited onto ZrO_2 could be transferred to the pyrolytically deposited carbon coating with different thermophysical properties was investigated. The University of Manchester supplied ZrO_2 kernels that were coated with porous carbon buffer layers deposited by CVD and dense pyrolytically deposited coatings (PyC layers) and had densities and carbon coating thicknesses similar to those of TRISO particles.

The surface of the coating shown in Figure 1-23 exhibits a similar structure to that of the sample shown in Figure 1-22 coated under similar conditions. The greater contrast is indicative of a higher surface roughness, which was confirmed through measurements in the 3D laser scanning microscope. The roughness of the coated specimen was 250 nm (versus 100 nm based on the image given in Figure 1-22). This is due to the higher initial roughness Ra = 350 nm of the PyC coating. The coating shows no signs of cracking,

delamination, or buckling, which are all associated with stresses or stress relief in the coatings.

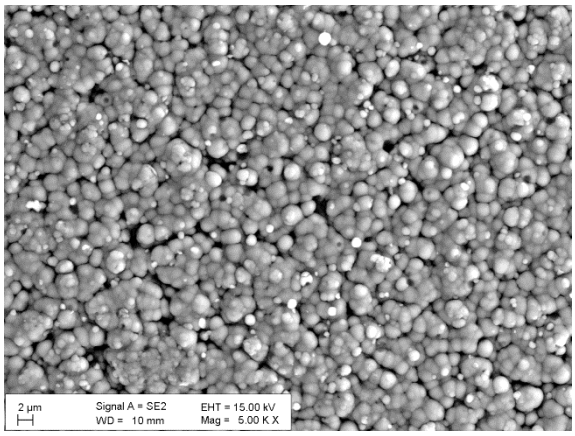

	C	O	Si	Si/C
Atom %	49.11	4.78	46.11	**0.94**

Figure 1-23: SEM micrograph (JRC-IET, Petten) of the surface of the SiC coating (left) and EDX analysis of the coating (right) for a coating thickness of approx. 3 µm and Ra = 250 nm, with t1 = 45 min, T1 = 350–500 °C, and p1= 10^{-4} mbar; and t2 = 45 min, T2 = 800 °C, and p2 = 10^{-1} mbar

A cross section through the fracture surface of the coating system is shown in Figure 1-24. The surface irregularities do not affect the density or homogeneity of the coating, which is firmly anchored to the carbon layer. The silver layer is clearly identifiable as an intense white, strongly reflecting region between the SiC coating and the carbon substrate. The silver also exhibited no bubble formation or delamination under the given temperature conditions. EDX analysis yielded an almost stoichiometric C/Si ratio of nearly 1 for the SiC coating.

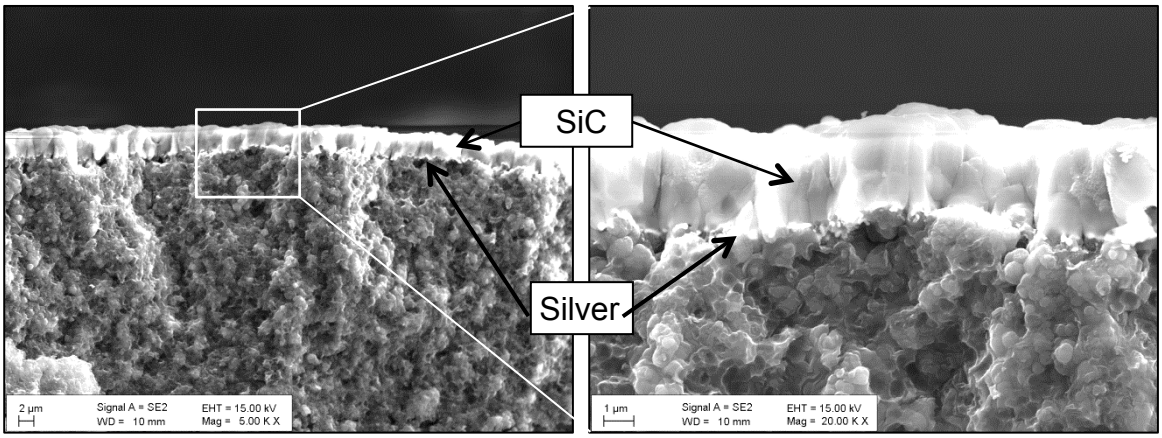

Figure 1-24: SEM micrographs (JRC-IET, Petten) of a cross section through the fracture surface of a PyC-silver-SiC coating system

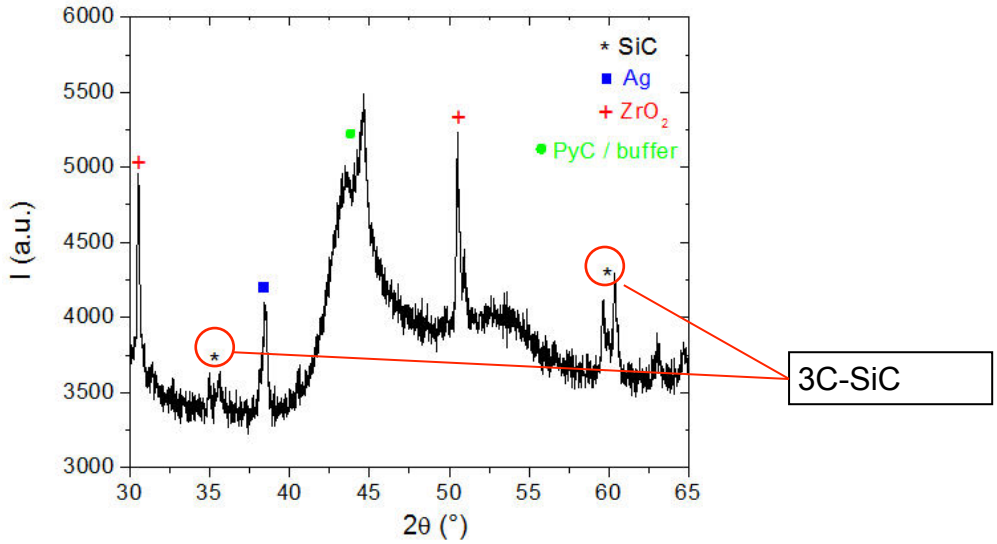

Figure 1-25: Grazing incidence X-ray diffraction pattern for a SiC-silver coating on PyC (Petten) with Tmax = 800 °C and a coating thickness of 3 µm

For these SiC-silver coating systems of thickness of about 3 µm deposited onto carbon at temperatures below 500 °C in a high vacuum for half of the total time and about 800 °C in an argon atmosphere for the remaining half of the time, crystalline components could be detected in the SiC coating. Figure 1-25 shows an XRD pattern in which the peaks of the CVD carbon coating, the ZrO_2 kernels, and the silver coating are clearly identifiable. Weaker, narrow peaks correspond to the crystalline phase of cubic SiC (3C-SiC) at 35.5° and evidently also at 60°. The relatively weak and broad peaks are indicative of a very fine crystalline structure with a grain size of a few nanometers.

1.6 Conclusions

Within the scope of the EU's ARCHER research project, the suitability of the PLD process for deposition of coatings or coating systems as components of the coating system for TRISO-coated particles was investigated to determine and quantify the coating integrity to prevent escape of radioactive fission products.

One aim of the work performed by TUD was to generate submicron-thick silver coatings on ZrO_2 particles to act as diffusion indicators, protected by thermally stable SiC coatings for subsequent CVD coating in a furnace at 1600 °C at the University of Manchester. For this purpose, a coating unit that uniformly moved the spheres to be coated in the vacuum chamber while maintaining their alignment to the target at a temperature of above 1000 °C for more than ten hours on a rotating graphite plate was successfully developed and tested.

Deposition of submicron-thick silver coatings was found to be easily possible. At a deposition rate of 0.5 nm/s, the coatings were nearly free of droplets and particulates. Under the given equipment-related conditions (pulse energy, pulse frequency, and vacuum level), the deposition rate could be increased to 3 nm/s. These coatings then primarily exhibited inhomogeneous coating thicknesses due to the presence of a large number of micron-sized droplets. The coatings were mainly free of cracks, adhered well to the substrate, and were dense. There were no signs of internal coating stresses.

Crystalline and hence thermally stable SiC coatings of thickness less than 1 µm could be generated in a high vacuum at deposition temperatures of ≥ 800 °C. Direct transfer of these results to silver-coated particles was hindered by the much less precise temperature measurement of the rotating spheres with a diameter < 1 mm and due to the use of higher chamber pressures. Crack-free high-temperature SiC coatings (≥ 800 °C) on silver were obtained through the combination of high-vacuum coating at temperatures of approximately 500 °C and a subsequent fine-vacuum coating at the crystallization temperature. These coatings were intact but exhibited bubbles. The ratio of silicon to carbon was significantly nonstoichiometric in some cases. Evacuation of the coating chamber and subsequent purging with 99.9999% argon three times yielded crack- and bubble-free coatings with a C/Si ratio approaching the stoichiometrice value of 1. Verfication of crystallinity in these low coating volumes was technically challenging. However, it can be concluded with certainty that these coatings exhibited nanocrystalline regions that could be assigned to cubic SiC.

Based on the findings obtained regarding coating of SiC on ZrO_2, it can be concluded that modification of the coating atmosphere can cause an increase in coating thickness and still retain the high adhesion and density of the coating.

1.7 Literature Cited

[1] H.M. Smith, A.F. Turner, Vacuum deposited thin films using a ruby laser, *Appl. Opt*. 4, 147 (1965)

[2] D. Dijkkamp, T. Venkatesan, X.D. Wu at al., Preparation of Y-Ba-Cu oxide superconductor thin films using pulsed laser evaporation from high T_c bulk material, *Appl. Phys. Lett.* 51, 619 (1987)

[3] D.B. Chrisey, G.K. Hubler, Pulsed laser deposition of thin films, *Wiley New York,* 1994

[4] H. Muto, S. Kamiya, T. Kusumori, Groth mechanism of a-SiC hetero-epitaxioal films by PLD as studie od the laser photon, pulse- width and substrates dependence, Optical Materials 23 (2003) 43

[5] C. Ristoscu, G. Scol, C. Ghica at al., Femtosecuond pulse shaping for phase and morphology control in PLD: Synthesis of cubic SiC, *Applied Surface Science* 252 (2006) 4857–4862

[6] T. V. Vekantesan, *Laser Ablation*, Springer, Berlin (1994)

[7] G. Reiße and S. Weissmantel, "Pulsed Laser Deposition of Hexagonal and Cubic Boron Nitride Films," *Applied Physics A (Suppl.),* vol. 69, pp. S749-S753, 1999

[8] D. Rost, Laserpulsabscheidung von superharten Schichten auf der Basis von diamantartigem Kohlenstoff und kubischem Bornitrid, Dissertation der TU Ilmenau, 2008

[9] N. V. Lyanguzov, V. E. Kaidashev, V. B. Shirkokov et al.: Magnetron and Pulsed Laser Deposition of Silverand gold nanoparticles and discontinuous films and their optical properties, Technical Physics 57 (2012) 1411-1416

[10] H. Nakashima, Y. Sasaki, R. Osozawa et al.: Surface enhanced infrared absorption spectra on pulsed laser deposited silver island films, Thin Solid Films, 536 (2013) 166- 171

[11] T. Zehnder, A. Blatter, A. Bächli: SiC films prepared by pulsed excimer laser deposition, Thin Solid Films, 241 (1994) 138-141

[12] M. Diegel, F. Falk, R. Hergt, H. Hobert and H. Stafast**:** Crystalline SiC thin film deposition by laser ablation: influence of laser surface activation; *Applied Physics A: Materials Science & Processing*, 1998, Volume 66, Number 2, Pages 183-187

[13] J. S. Pelt, M. E. Ramsey, S. M. Durbin: Characterization of crystalline SiC films grown by pulsed laser deposition, Thin Solid Films 371 (2000) 72-79

[14] T. Kusumori, H. Muto, M. E. Brito: Contraol of polytoype formation in silicon carbide hereroepitaxial films by pulsed-laser deposition, Applied Physics Letters, 84, 8 (2004) 1272- 1274

[15] A. *Keffous,K. Bourenane, M. Kechouane, at al.:* **Morphological, structural and optical properties of thin SiC layer growth onto silicon by pulsed laser deposition;** *Vacuum, Volume 81, Issue 5 (2007) 632*

[16] F. Neri, F. Barreca, S. Trusso: Excimer laser ablation of silicon carbide ceramic targets; *Diamond and Related Materials*, Volume 11, Issue 2 (2002) 273

[17] Y.H Tang, T.-K. Sham, D. Yang, L. Xue Tang: Preparation and characterization of pulsed laser deposition (PLD) SiC films*; Applied Surface Science*, Volume 252, Issue 10, 15 March (2006) 3386

[18] M. Tabbal, A. Said, E. Hannoun et al.: Amorphous to crystalline phase transition in pulsed laser deposited silicon carbide, Applied Surface Sciende 253 (2007) 7050- 7059

[19] G. Monaco, D. Garoli, M. Natali et al.: Synthesis of heteroepiytaxial 3C-SiC by means of PLD, Applied Physics A (2011) 225-231

[20] A. Chauhan, W. Moran, S. Ge, at al: Pulsed laser deposition of silicon carbide on heat resistant materials; *Scripta Materialia*, Volume 52, Issue 8 (2005) 735

[21] M. Kracker, C. Worsch, C. Bocker et al.: Optical properties of dewetted thins silver/gold multilayer films on glass substrates, Thin Solid Films, 539 (2013) 47-54

[22] J.C. Alonso, R. Diamant, P. Castillo et al.: Thin films of silver nanoparticles depositied in vacuum by pulsed laser ablation using an YAG:Nd laser, Applied Surface Sciende, 255 (2009) 4933- 4937

[23] C.A. Smyth, I. Mirza, J.G. Lunney et al.: Surface-enhanced Raman spectroscopy (SERS) using Ag nanoparticle films produced by pulsed laser deposition, Applied Surface Science, 264 (2013), 31-35

[24] E. Fazio, F. Neri, P.M. Ossi et al.: Growth process of nanostructured silver films pused laser ablated in high-pressure inert gas, Applied Surface Science, 255 (2009), 9676-9679

[25] H. Nakashima, Y. Sasaki, R. Osozawa et al.: Surface enhanced infrared absorption spectra on pulsed laser deposited silver island films, Thin Solid Films, 536, (2013) 166-171

[26] P. DeVasConCellos, S. Bose, H. Heyenal et al.: Antimicrobial particulate silver coatings on stainless steel implants for fracture management, Materials Science and Engineering: C, 32, Issue 5 (2012) 1112-1120

[27] S. Svensson, F. Suska, L. Emanuelsson, A. Palmquist et al.: Osseointegration of titanium with an antimicrobial nanostructured noble metal, Nanomedicine; Nanotechnology, Biology and Medicine, 9, Issue 7 (2013) 1048-1056

[28] J. Podporska-Carroll, B. Quilty, R. Devery: Non-cytotoxic and antimicrobial plasma sprayed coatings for orthodaedic application, Materials Letters, 112 (2013) 54-57

[29] Young-Woo Lee et al.: Development of HTGR-coated particle fuel technology in Korea; Nuclear Engineering and Design 238 (2008) 2842-2853

[30] Hrovat, M., Schulten, R., Grosse, K-H.: Kugelförmiges Brennelement und dessen Herstellung für gasgekühlte Hochtemperatur-Kugelhaufen-Kernreaktoren (HTR); DE102006040309A1, 13.3.2008

[31] Charollais, F., Fonquernie, S. at al: CEA and AREVA R&D on htr fuel fabrication and presentation of the CAPRI experimental manufacturing line; Nuclear Engineering and Design 236 (2006) 534-542

[32] Reitano, R.; Baeri, P.; Marino, N.: Excimer laser induced thermal evaporation and ablation of silicon carbide, Applied Surface Science, 96-98 (1996) 302-308

[33] Informationszentrum Technische Keramik: Brevier Technische Keramik, Fahner Verlag 1999

[34] Lensa, W.: Internationale Entwicklungsprogramme zum Hochtemperaturreaktor.http://www.vdi.de/fileadmin/vdi_de/redakteur_dateien/get_dateien/Hochtemperaturreaktor-Fachvortrag.pdf 2007

[35] Hofmann, H.; Spindler, J.: Verfahren der Oberflächentechnik, Fachbuchverlag Leipzig, 2004

[36] Reflexionsgrad aus Wikipedia, der freien Enzyklopädie, de.wikipedia.org

[37] Shayan, A. R, Poyraz, H. P.: Laser Absorption for Si and SiC: https://www.wmich.edu/mfe/mrc/pdf/Amir%20and%20Bogac_Laser%20Absorption%20for%20Si%20and%20SiC_10-24-2008.pdf, Western Michigan University, 2008

[38] Gmelin, Handbook of Inorganic Chemistry, Si Sppl. Vol. B2 Compounds, Springer, 1984

[39] A. Anders, "A structure zone diagram including plasma-based deposition and ion etching," *Thin Solid Films,* vol. 518, pp. 4087-4090, 2010.

[40] D. Smith, Thin-Film Deposition - Principles and Practice, Library of Congress, 1995

[41] A.-M. Reinecke, M. Lustfeld, W. Lippmann, A. Hurtado: Creation of leak-proof silicon carbide diffusion barriers by means of pulsed laser deposition, Nuclear Engineering and Design, 271 (2014) 92-98

[42] C. Davis, "A simple model for the formation of compressive stress in thin films by ion bombardment," *Thin Solid Films,* vol. 226, pp. 30-34, 1993.

[43] R. Koch, "Stress in Evaporated and Sputtered Thin Films - A Comparison," *Surface & Coatings Technology,* vol. 204, pp. 1973-1982, 2010.

[44] T. Zehnder, A. Blatter and A. Bächli, "SiC films prepared by pulsed excimer laser deposition," *Thin Solid Films,* vol. 241, pp. 138-141, 1994.

[45] Gmelin, Handbook of Inorganic Chemistry, Boron Suppl. Vol. 2 Elemental Boron, Boron Carbides, Springer, 1981

[46] X.Q.Yan, W.Li, T. Goto at al., “Ramen spectroscopy of pressure-induced amophous boron carbide”, Applied Physics Letters 88, 131905 (2006)

[47] Advances in Ceramics - Characterization, Raw Materials, Processing, Properties, Degradation and Healing, Edited by Costas Sikalidis, ISBN 978-953-307-504-4, 382 pages, Publisher: InTech, Chapters published August 01, 2011 under CC BY-NC-SA 3.0 license DOI: 10.5772/933

[48] S.C.M. Knoll, “Elektrophoretische Formgebung von nanoskaligem Zirkondioxid”, Dissertationsschrift, Universität des Saarlandes, 2001

[49] A.-M. Reinecke, M. Lustfeld, W. Lippmann, A. Hurtado: Creation of leak-proof silicon carbide diffusion barriers by means of pulsed laser deposition, in: Nuclear Engineering and Design, vol. 271, pp. 92-98 (2014)

2 Fundamental study of silver and silicon carbide at the University of Manchester

The continuous release of the metastable silver nuclide Ag-110m from otherwise fully intact TRISO fuel at moderate temperatures poses a threat towards the safe operation of HTRs. Even though this phenomenon has been described decades ago the mechanism of silver release through the SiC coating has not been understood so far and a number of different explanations have been suggested without reaching an overall agreement.

The work conducted at the University of Manchester within the Archer project follows two approaches to study the interaction of silver and silicon carbide in its fundamentals. At first, pellets consisting of silver and silicon carbide powders were fabricated, which were subsequently heat-treated at temperature well above the regular reactor operating conditions. This ensured an increased reaction rate along the large contact areas of the two compounds, allowing a better observation of any interactions. Since treatment temperatures were well above the melting point of metallic silver, significant evaporation occurred, but sufficient metallic silver was still found within the pellets. This rather novel and unconventional approach offered a few advantages towards the study of TRISO fuel directly. Firstly, the possibility to use SiC powders of the alpha and beta modification as starting materials gained more insight into the reaction mechanism as described further on. Secondly, the difficult and time consuming sample fabrication when working with SiC coatings in TRISO particles can be circumvented. Based on the experimental findings and thermodynamic considerations a new model describing the migration mechanism in silver through silicon carbide has been proposed. This investigation however does not take microstructural characteristics as grain morphology into account, which are known to play a significant role in the release rate observed in irradiated fuel (1). However, a significantly improved understanding of the interactions could be gained, which promises to be very beneficial for future work.

The second part was a trial study of entrapping a thin layer of silver between two SiC coatings in a TRISO particle. Due to the experimental difficulties in preparing robust coatings by laser deposition (see above) a route of ceramic processing was taken to prepare silver containing TRISO particles. This approach proved to be experimentally challenging as well and only a small number of particles were successfully heat-treated

and analysed. Observations made in these experiments were found to be in good agreement with the model derived from the more fundamental powder study.

Subsequently we summarize the experiments undertaken here and give a detailed description of the thermodynamic calculations. Finally, the proposed model for the silver migration mechanism in SiC is presented. The work was published in form of a full length article in the Journal of the American Ceramic Society and presented at the conference on Advanced Ceramics and Composites (Daytona Beach Florida, 2014) (2). A list of the resulting publications is provided at the end of this document.

2.1 Experimental procedure

Two types of samples were prepared:

SiC-Ag powder composite pellets; **silver powder was added to silicon carbide powder of the α or β-modification in the weight ratio of 9:1. The powders were mixed with the addition of acetone inside a speed mixer, dried in warm air and cold-pressed into pellets. After thermal treatment using a tube furnace and vacuum atmosphere at 1450°C for different durations (see**

- Table 5) all samples were mounted into epoxy resin for analysis by microscopy and Raman Spectroscopy.
- **TRISO particles containing a trapped silver layer**; simulated TRISO particle fuel was prepared by fluidized bed chemical vapour deposition (FBCVD) using zirconia spheres of 500 µm diameter (PI-KEM Ltd, Staffordshire, UK) as a substrate in the FBCVD coating facility at Manchester. Initially, two layers of pyrolytic carbon and one of silicon carbide were deposited; subsequently a thin silver film was brought directly onto the silicon carbide layer before depositing another coating of silicon carbide by FBCVD. Heat treatment was done in low pressure argon atmosphere for 10 hours at 1800°C. The sample was mounted in copper containing resin and polished to the approximate cross-section of the particle for microscopy and Raman Spectroscopy.

Table 5: Composition and thermal treatment conditions for the samples in this study

Sample ID	Sample composition	Thermal annealing temperature (°C)	Annealing duration (h)
A3	10 wt% α-SiC[2] + 90 wt% Ag[1]	1450	3
B1	10 wt% β-SiC[3] + 90 wt% Ag[1]	1450	1
T10	TRISO particle containing Ag-layer	1800	10

[1] silver powder from Alfa Aesar, UK, 99.9%, 0.7 – 1.3 µm

[2] α-SiC powder from Goodfellow, UK, 98.7%, 75 µm

[3] β-SiC powder from Alfa Aesar, UK, 99.8%, 1 µm

- **Sample characterisation;** Samples were examined using a scanning electron microscope coupled with an energy-dispersive X-ray spectrometer (EDX) (Philips XL 30 FEG-SEM; Eindhoven, the Netherlands) using 8 kV as accelerating voltage.

Raman spectroscopy was done using the 514.5 nm line of an Argon laser in a Renishaw Raman microscope 1000 system. A fifty-times objective lens was used.

2.2 Observations and experimental results

Within this work a number of samples had been prepared and analysed and a representative selection is presented here. The observations are described and illustrated with SEM micrographs and Raman spectra.

2.2.1 Reaction at the interface of the SiC-Ag powder pellets

The thermal treatment temperature of the powder composite pellets was sufficiently high to cause a partial evaporation of silver in all samples, but this effect was more pronounced for longer annealing durations. Still all samples contained a separate silver and silicon carbide phase after thermal treatment and a reaction zone along the interphase of these two compounds could be observed.

As seen in SEM micrographs of sample B1 (Figure 2-1a) silver and silicon carbide are generally well dispersed within the pellet with some silver bubbles forming along the outside rim. This accumulation of silver contained around 1.5 ± 0.1 at% silicon inside as detected by EDX measurements (Figure 2-1b,c). The carbon peak seen in the spectrum of Figure 2-1c is likely due to the thin carbon coating of the sample surface required for SEM characterisation. High magnification micrographs of the area containing SiC and silver show that some silver particles are fully surrounded by SiC (Figure 2-1d,e). The SiC particles were bonded to each other suggesting that some chemical reaction had occurred, since sintering of SiC generally requires much higher temperatures.

Analysis by Raman spectroscopy had been carried out on the surface of that sample with the results presented in Figure 2-1f. For comparison that graphs also gives the Raman spectrum of pure β-SiC powder without any thermal treatment. The peaks relating to silicon carbide remain almost identical in the two spectra. The two first order peaks of cubic SiC are clearly visible (LO and TO band at 796 and 972 cm^{-1}, respectively). The untreated SiC also shows the second order SiC peaks and only minor signs of carbon impurities, whereas in sample B1 carbon peaks become dominant in that part of the spectrum. The D and G band of carbon are both well developed, revealing that carbon is present in the form of only little textured graphite.

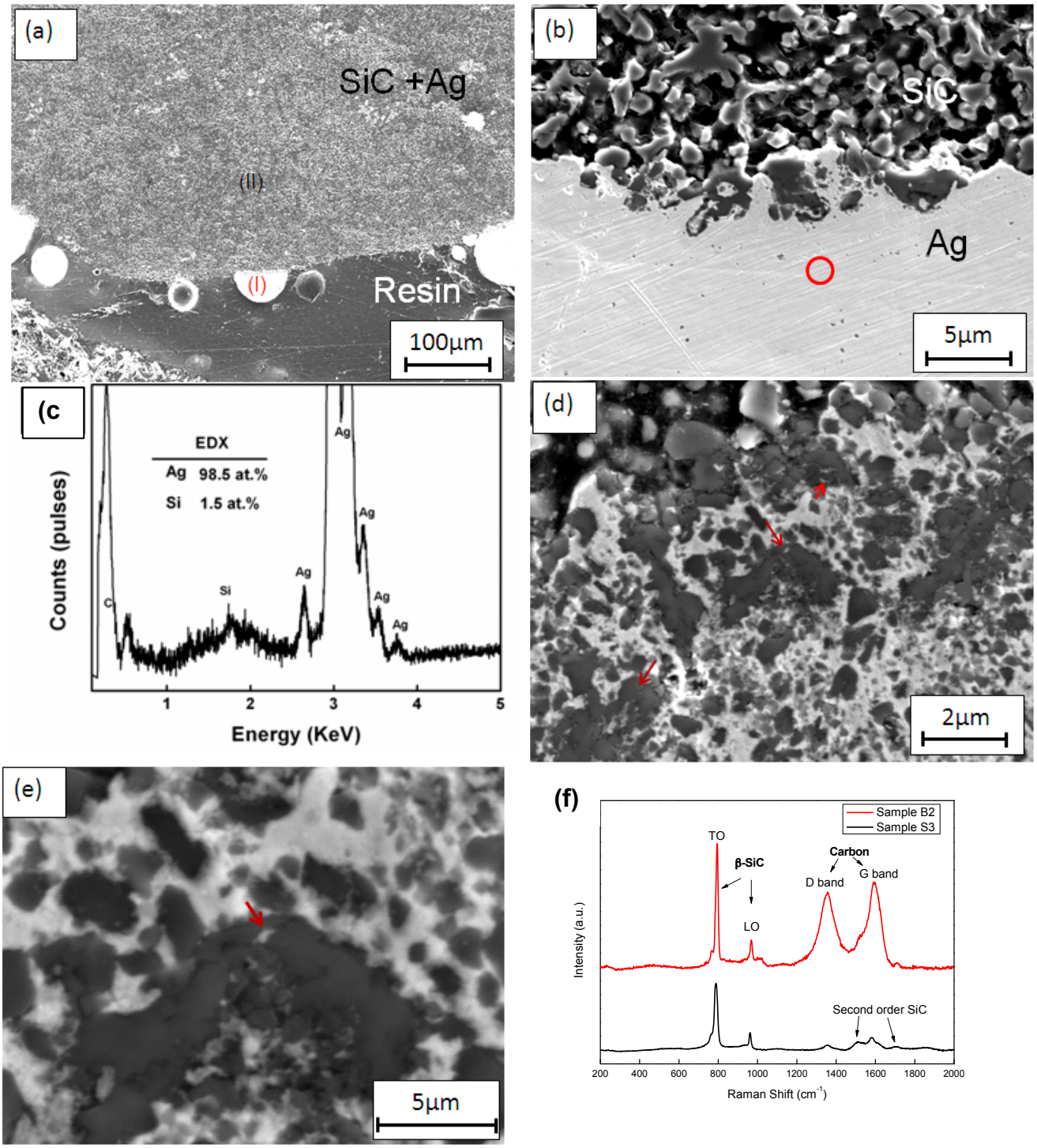

Figure 2-1: **Sample B1; (a) SEM micrographs showing the composite pellet in low magnification; (b) is a magnified view of area (I) in (a); (c) gives the EDX spectrum of the red circles area in (b); (d) and (e) show a high magnification view of area (II) in (a); (f) Raman spectrum of B1, S3 is pure β-SiC powder without thermal treatment.**

Following this initial test it appeared that a reaction occurs along the interface of silicon carbide and silver. To achieve a better understanding another sample was prepared replacing the finely grained β-SiC by large particles of α-SiC and a slightly prolonged heat

treatment at the same temperature. The SEM micrograph in Figure 2-2a shows one large α-SiC particle and the surrounding silver phase. A thin layer on the surface of the particle however exhibited a different contrast in the micrograph (see red arrows in Figure 2-2a). Similarly to the earlier tests using β-SiC also in sample A3 the silver phase contained a detectable amount of silicon. EDX measurements taken within the silver phase at some distance to the SiC particle showed an identical silicon concentration of 2.01 at%.

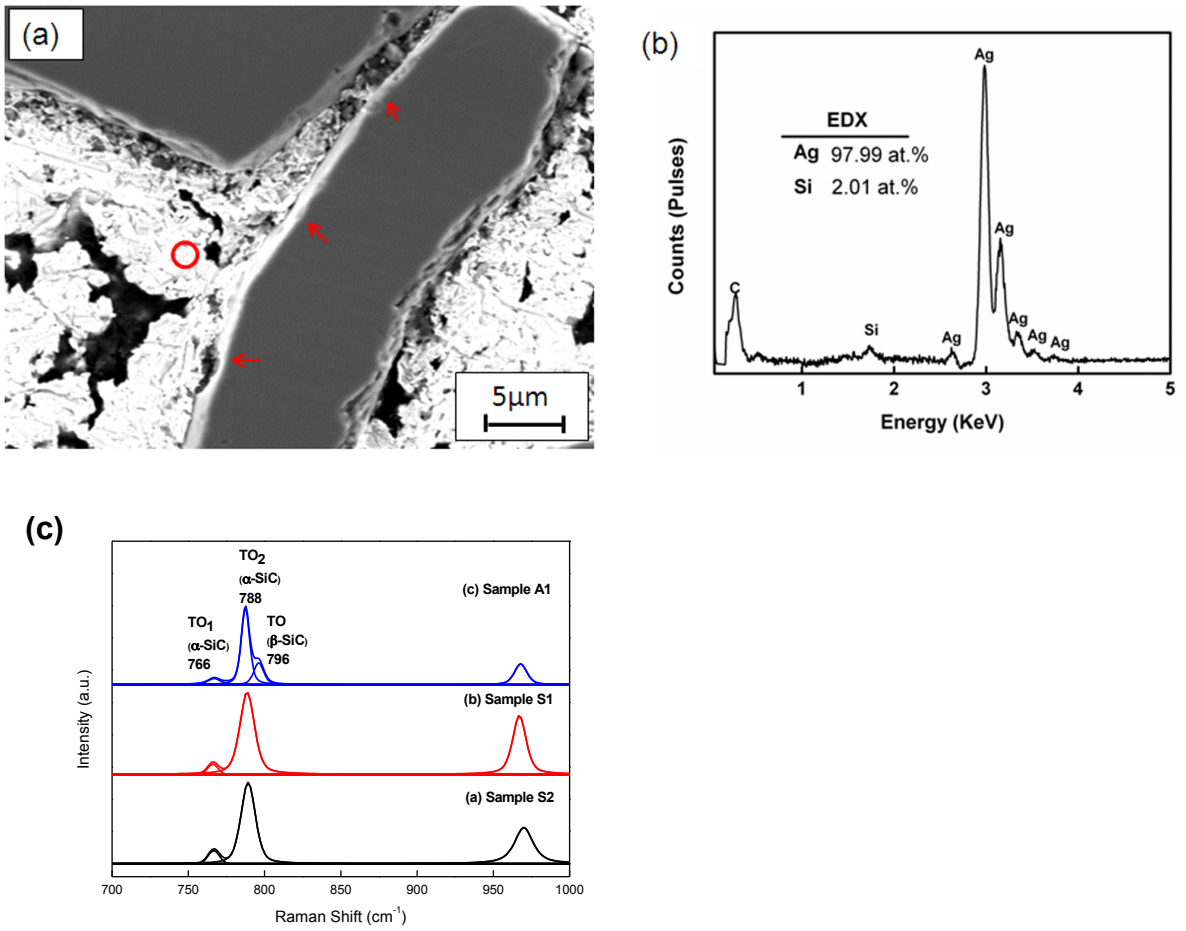

Figure 2-2: Sample A3; (a) SEM micrograph the red arrows point towards the thin film on the particle surface; (b) EDX measurement of the red circle area in (a); (c) Raman spectra of sample A3, S1 and S2 are α-SiC powders pristine and after heat treatment (48 h at 1450°C), respectively.

Raman spectroscopy of this sample showed that the thin film formed on surface of the α-SiC particle is in fact β-SiC. In Figure 2-2c the Raman spectra of sample A3 is given and for comparison the same analysis had been conducted on the pristine α-SiC and after heat treatment for 48 hours at 1450°C. Without the presence of silver the Raman spectrum shows only the bands relating to 6H-SiC (TO_1 and TO_2 at 766 and 788 cm^{-1}). For this SiC polytype the TO band is split into two separate peaks that are both a lower wavenumbers

than the TO band of 3C-SiC. The second order bands are visible, too and no trace of carbon impurities could be seen. The Raman spectrum of sample A3 however showed a detectable amount of cubic SiC in addition to the hexagonal phase (blue spectrum in Figure 2-2c).

Concluding from these observations it is inferred that at high temperatures SiC reacts with silver by forming a silver-silicon alloy. Carbon remains as a separate phase in the form of graphite. The newly formed film visible in the SEM characterisation of A3 is cubic SiC that is formed following this reaction.

2.2.2 TRISO Particle with entrapped silver layer

One example of the TRISO particle with an entrapped thin layer of silver between two SiC coatings is shown in Figure 2-3a. Due to the different deposition conditions the microstructure and stoichiometry of the two SiC layers varied significantly. The inner SiC layer has the more typical grain morphology of TRISO particle coatings and shall therefore be investigated more in detail here. This microstructure consists of elongated grains that are a few microns long and have a width of some hundred nanometres. The coating thickness is about 43 µm and Raman spectroscopy showed that the SiC is fully stoichiometric with a low concentration of stacking faults.

After thermal treatment at 1800°C a large reaction zone is observed. As seen in Figure 2-3c the silver had penetrated about 20 µm into the SiC coating and the microstructure of the SiC was completely reformed. Some agglomerates of silver were found in between large SiC grains. The magnified view (Figure 2-3d) shows that the grains of the unreacted zone are still of a similar size and shape as before annealing. In the reaction zone the grains are large (~20 µm) and have no particular orientation or shape. These observations suggest that silver helps the recrystallization of SiC. Raman spectra taken in the penetrated and non-penetrated zone are identical and show bands relating to cubic SiC exclusively.

Figure 2-3e and f illustrate the different shapes of silver agglomerates found within the SiC coating. Different morphologies could be detected:

(1) a wedge-shape silver agglomerate along the SiC grain boundary with a dihedral angle of 61.4° (Figure 2-3f);
(2) finger-shaped silver inclusions (area V in Figure 2-3e);

(3) small spherical dots inside of large SiC grains (area III in Figure 2-3e). The distance between the silver dots is around 1 µm and thus in a similar range as the grain size of the original coating layer.

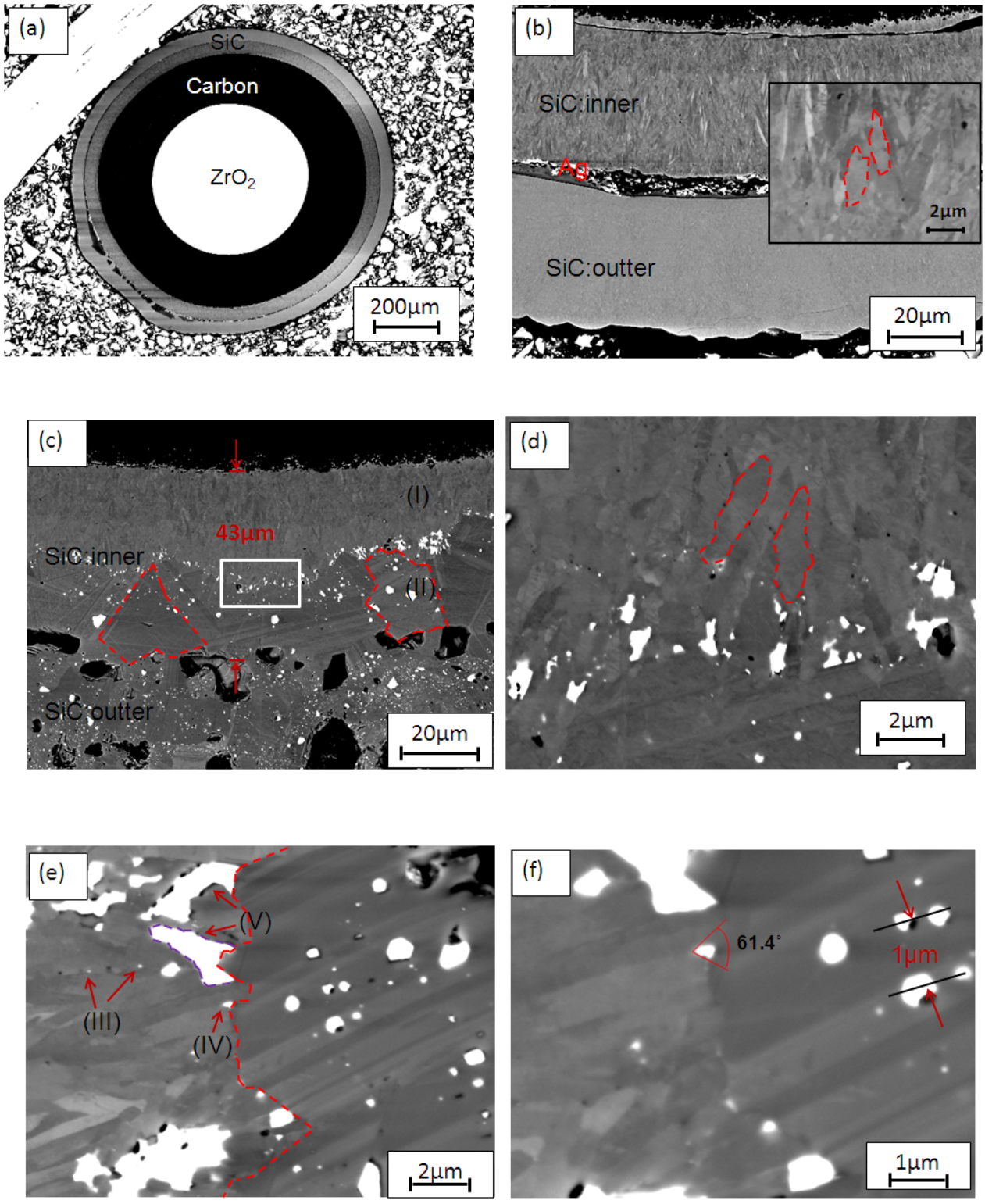

Figure 2-3: **TRISO particle with entrapped silver layer; (a) SEM micrograph showing the whole sample T10 before thermal treatment; (b) larger view of the two SiC coatings, the inset shows the microstructure of the inner SiC layer; (c) similar area as in (b) after thermal treatment showing a large reaction zone; (d) is the enlarged view of the rectangular area in (c); (e) and (f) high magnification micrographs showing the different silver agglomerates within the SiC microstructure.**

2.3 Discussion of experimental results

The experiments described above show that silver in its liquid state reacts with silicon carbide of the α and β-modification. Silver dissolves SiC by forming a silver-silicon alloy and carbon as a second phase. However, new β-SiC is formed by a recombination of silicon and carbon. In SiC coatings of TRISO particles silver agglomerates were found along the SiC grain boundaries that exhibited either a wedge or finger shape. Recrystallization of SiC occurred that led to the formation of bigger SiC grains that were about one magnitude larger than the grains in the original coating.

The thermodynamics of the system silver and SiC were assessed here to explain these findings and a model for the silver migration mechanism through SiC in TRISO particles is subsequently proposed.

2.3.1 Thermodynamic equilibrium calculation

The equation for the reversible reaction of silver and SiC is given as:

$$(1-x)Ag(l) + x\,\beta - SiC(s) \leftrightarrow Ag_{(1-x)} - Si_{(x)}(l) + xC(s) \qquad \textbf{Equation 2.1}$$

Liquid silver reacts with β-SiC by forming a liquid silver-silicon alloy and carbon as a separate phase. Recrystallization of SiC occurs when a fraction of the silicon recombines with carbon, thus this reaction is reversible. According to the silver-silicon phase diagram silver-silicon alloys with a silicon content up to 11 at% have melting points between 835°C and 961°C(3). During reactor operation the fuel particles are at a temperature exceeding the silver melting point (961°C), thus silver will be in its liquid form.

The solubility of carbon in silver is generally low, so the thermodynamic equilibrium of the reaction can be described by Equation 2.2:

$$\Delta G = \sum x_i \cdot G_i = G_{Ag_{(1-x)}Si_{(x)}(l)} + xG_{C(s)} - (1-x)G_{Ag(l)} - xG_{\beta-SiC(s)} \qquad \textbf{Equation 2.2}$$

Here x is the mole fraction of silicon in the silver phase in Equation 2.1. Based on the regular solution model, the Gibbs formation energy for the silver-silicon allow is expressed by:

$$G_{Ag_{(1-x)}Si_{(x)}(l)} = (1-x)G^0_{Ag(l)} + x\left(G^0_{Si(s)} + \Delta G_{Si(s\to l)}\right) + RT(x\cdot lnx + (1-x)\ln(1-x)) + \Delta^E G \quad \text{Equation 2.3}$$

$\Delta^E G$ is the excess Gibbs free energy of liquid silicon-silver alloys. This term is neglected here, because ideal solution behaviour in the silver-silicon system can be achieved as long as the silicon content is below 10 at%. This equation is further simplified by dropping the term (1-x)ln(1-x) as it becomes very small for small x and hence Equation 2.2 can be rewritten as:

$$\Delta G = x(G^0_{Si(s)} + \Delta G_{Si(s\to l)} + RTlnx + G^0_{C(s)} - G^0_{\beta-SiC(s)}) \quad \text{Equation 2.4}$$

$\Delta G_{Si\to l}$= 51130 -30.34 T(J/mol) for temperatures below the melting point of silicon at 1414°C and the expression becomes zero for temperatures above.

In Equation 2.4 the Gibbs energy depends on the temperature and the more fraction of silicon. Assuming thermodynamic equilibrium the Gibbs energy is zero and a relation between the mole fraction of silicon and the system temperature can be calculated using Equation 2.5:

$$\mathrm{x} = exp\left(\frac{G^0_{\beta-SiC(s)} - G^0_{Si(s)} - \Delta G_{Si(s\to l)} - G^0_{C(s)}}{RT}\right) \quad \text{Equation 2.5}$$

This relationship between temperature and solubility of silicon in liquid silver is illustrated in Figure 2-4. The experimental data obtained by EDX measurements on the composite samples A3 and B1 of 1.5 at% are in good agreement with the value calculated according to the theory described above of 1.66 at% at 1450°C. Evidently, the solubility of silicon in silver is strongly temperature dependent.

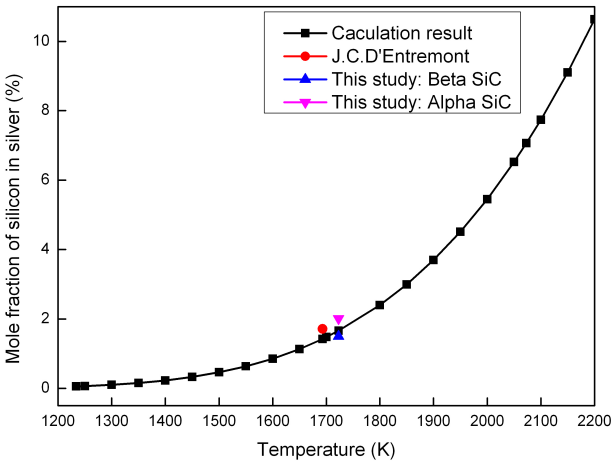

Figure 2-4: Temperature dependence of silicon solubility in silver-silicon alloys; the black line is the theoretical value calculated from Equation 2.5, blue and pink are the data points measured by EDX as described in the experimental section, and the red point is experimental data from literature (4).

2.3.2 SiC grain boundary wetting by silver-silicon alloys

Micrographs of the silver containing TRISO particle have shown that silver agglomerates were present in finger or wedge shape along the SiC grain boundaries, which suggests that a wetting mechanism of the silver-silicon alloy in the SiC grains is the cause for penetration. This mechanism and its driving force are assessed thermodynamically here.

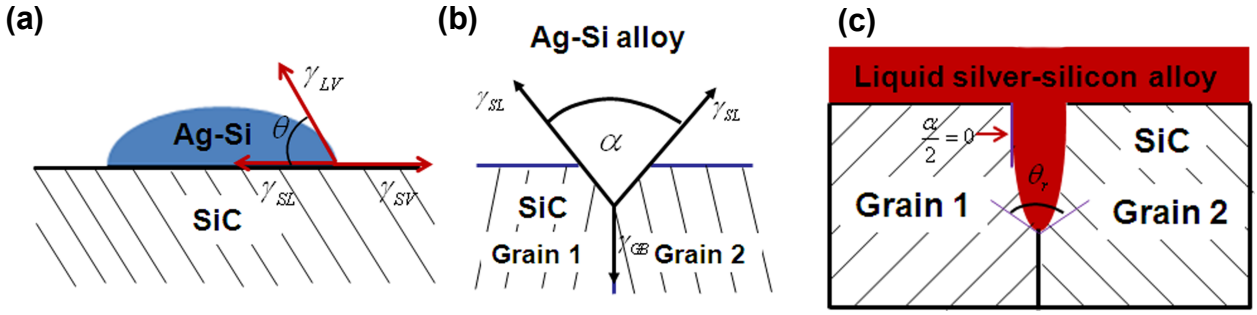

Figure 2-5: Schematic graphs in metal-ceramic system in equilibrium state taken from Ref (5,6) and adjusted for the Silver-SiC system here defining the angles used in the equations below; (a) contact angle (θ); (b) dihedral angle (α); (c) wetting of SiC by silver-silicon alloy.

Young's equation defines the contact angle (α) of liquid silver or the silver-silicon alloy:

$$\gamma_{SV} = \gamma_{SL} + \gamma_{LV} \cos\theta$$ **Equation 2.6**

γ_{SL} is the interfacial tension between the liquid metal and SiC, γ_{SV} is the surface tension of SiC and γ_{LV} is the surface tension of liquid metal. For θ < 90° the liquid metal wets the solid ceramic surface. The dihedral angle (α) is then expressed by Equation 2.7 with γ_{GB} as the grain boundary energy of SiC. For α > 120° ($\gamma_{GB} > \gamma_{SL}$) the SiC ceramic is wetted by the liquid metal.

$$\gamma_{GB} = 2\gamma_{SL} \cos\frac{\alpha}{2}$$ **Equation 2.7**

Earlier it had been found that the contact angle of silver and SiC is too high to cause wetting, however even small amounts of dissolved silicon within the silver phase reduce the contact angle significantly and hence cause wetting to occur.

From SEM micrographs a value of 61.4° for the dihedral angle of the wedge-shape silver agglomerate along the SiC grain boundary was measured (see Figure 2-3f). Assuming that the SiC grain boundary energy is lower than twice the interfacial energy between the silver-silicon alloy and SiC Equation 2.7 can be rewritten as:

$$\alpha = 2arc\cos\left(\frac{\gamma_{GB}}{2\gamma_{SL}}\right) \qquad \textbf{Equation 2.8}$$

Following this equation and with values of 1.49 J/m^2 and 2.58 J/m^2 for the interfacial tension of the liquid metal and SiC and the SiC grain boundary energy, respectively, the angle is calculated as 60°, which is in good agreement with the experiment.

Finger-shaped silver agglomerates were found along the SiC grain boundaries (see area V Figure 2-3e). The mechanism of their formation is described in Figure 2-5c. The reaction is driven by the imbalance force between γ_{GB} and the projection force of the interfacial tension $\left(2\gamma\cos\left(\frac{\theta_r}{2}\right)\right)$:

$$F = \gamma_{GB} - 2\gamma_{SL}\left(\frac{\theta_r}{2}\right) \qquad \textbf{Equation 2.9}$$

2.3.3 Silver Migration mechanism in SiC coatings of TRISO fuel

An illustration of the proposed model is given in Figure 2-6. Initially molten silver is in direct contact with SiC surface. When silicon is dissolved into silver and forming a silver silicon alloy, the contact angle is decreased sufficiently to cause wetting along the SiC grain boundaries. This reaction is driven by the imbalance force between the grain boundary energy and the projection force of the interfacial tension of liquid silver-silicon alloy and SiC. Recrystallization of SiC occurs along the trailing edge of the reaction zone forming large SiC grains.

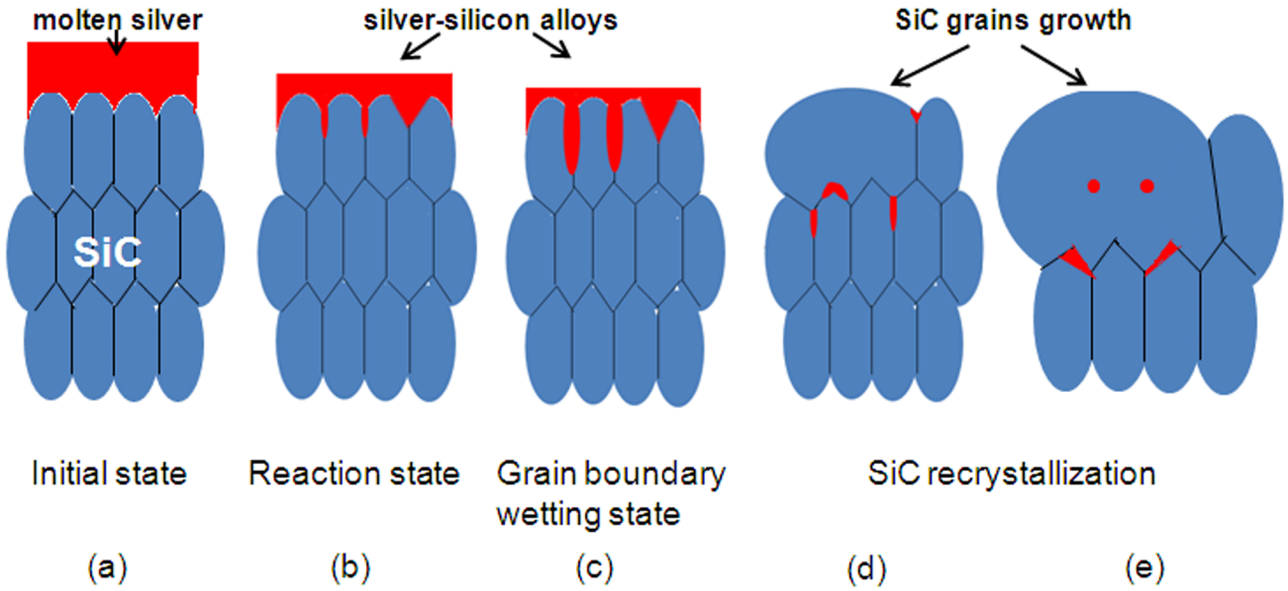

Figure 2-6: Model for silver migration mechanism in SiC coating of TRISO fuel; (a) initial state; (b) reaction state; (c) grain boundary wetting; (d) and (e) SiC recrystallization.

2.4 Summary and Conclusions

The experiments and calculations show that in its liquid state silver dissolves SiC by forming a silver-silicon alloy and a separate carbon phase. This reaction is partly reversible and independent of the original SiC polytype leads to the formation of β-SiC. Tests including silver containing TRISO particles showed that silver penetrates the SiC coating rapidly and in large quantities causes recrystallization of SiC grains.

This proposed mechanism is completely novel approach to look at the cause of silver release from intact SiC coatings in TRISO fuel. Former reports have focussed on diffusion theories or vapour transport models through nanocracks in SiC. A migration mechanism that is founded on a reaction might be unavoidable, but still could be mitigated by a careful engineering of the SiC microstructure since grain boundary characteristics will influence the silver release rates observed in irradiation experiments.

List of Presentations and publications resulting from this research

- Xin Geng, Fan Yang, Nadia Rohbeck and Ping Xiao. *An Original Way to Investigate Silver Migration Through Silicon Carbide Coating in TRISO Particles*. J. Am. Ceram. Soc. 2014 Mar 14;97(6):1979–86.

- Oral presentation at the 38th International Conference on Advanced Ceramics and Composites, *Proceedings in preparation.*

References

1. Petti DA, Buongiorno J, Maki JT, Hobbins RR, Miller GK. Key differences in the fabrication, irradiation and high temperature accident testing of US and German TRISO-coated particle fuel, and their implications on fuel performance. Nucl Eng Des. 2003;222:281–97.

2. Geng X, Yang F, Rohbeck N, Xiao P. An Original Way to Investigate Silver Migration Through Silicon Carbide Coating in TRISO Particles. Vance L, editor. J Am Ceram Soc. 2014 Mar 14;97(6):1979–86.

3. Olesinski RW, Gokhale AB, Abbaschian GJ. The Ag-Si (Silver-Silicon) system. Bull Alloy Phase Diagr. Springer US; 1989 Dec;10(6):635–40.

4. d'Entremont JC, Chipman J. The Free Energy of Silicon Carbide from its Solubility in Molten Silver. J Phys Chem. 1963 Feb 1;67(2):499–501.

5. Nikolopoulos P. Surface, grain-boundary and interfacial energies in Al2O3 and Al2O3-Sn, Al2O3-Co systems. J Mater Sci. 1985 Nov;20(11):3993–4000.

6. Glickman EE, Nathan M. On the kinetic mechanism of grain boundary wetting in metals. J Appl Phys. AIP Publishing; 1999;85(6):3185–91.